



Calculation of predictions for non-identical particle correlations in heavy ions collisions at LHC energies from hydrodynamics-inspired models

MASTER OF SCIENCE THESIS

Author:
Mateusz Wojciech Gałażyn

Supervisor:
Prof. Adam Kisiel

Warsaw, 30th November 2014



Wyznaczenie przewidywań teoretycznych dla korelacji cząstek nieidentycznych w zderzeniach ciężkich jonów przy energiach LHC w modelach opartych na hydrodynamice

PRACA MAGISTERSKA

Autor:
Mateusz Wojciech Gałażyn

Promotor:
dr hab. inż. Adam Kisiel, prof. PW

Warszawa, 30 listopada 2014

1 Abstract

2 This thesis presents results of two-particle momentum correlations analysis
3 for different kinds of particles produced in heavy ion collisions. The studies
4 were carried for the data from lead-lead collisions at the centre of mass
5 energy $\sqrt{s_{NN}} = 2.76$ TeV simulated in the THERMINATOR model using the
6 (3+1)-dimensional hydrodynamic model with viscosity. Analysis was performed
7 for the three particle kinds: pions, kaons and protons for the collisions in eight
8 different centrality ranges.

9 The THERMINATOR model allows to perform statistical hadronization of
10 stable particles and unstable resonances from a given hypersurface which is
11 followed by the resonance propagation and decay phase. The four-dimensional
12 hypersurface is coming from the calculations performed on a basis of relativistic
13 hydrodynamic framework with the viscosity corrections.

14 One can investigate space-time characteristics of the particle-emitting source
15 through two-particle interferometry using experimental observables. The
16 experimental-like analysis of the data coming from a model calculations yields
17 a possibility to test the hydrodynamic description of a quark-gluon plasma.
18 This thesis concentrates on the verification of the prediction of appearance of
19 femtoscopic radii scaling with the transverse mass.

20 The three dimensional correlation functions were calculated using spherical
21 harmonics decomposition. One can use this approach to perform calculations
22 with lower statistics and the visualization of results is much easier. The calcu-
23 lated correlation functions show expected increase of a correlation for pions and
24 kaons at the low relative momenta of a pair. For the protons at the same mo-
25 mentum region, the decrease occurs. The transverse pair momentum and cen-
26 tralitity dependence on a correlation function is observed. In order to perform the
27 quantitative analysis of this influence, the fitting of theoretical formula for cor-
28 relation function was performed. The femtoscopic radii calculated in the LCMS
29 and PRF are falling with the transverse mass m_T . To test the scaling predicted
30 from the hydrodynamics, the power law was fitted $\alpha m_T^{-\beta}$. The radii calculated
31 for pions, kaons and protons in the LCMS are following the common scaling. In
32 case of the PRF no such scaling is observed. To recover the scaling in the PRF, the
33 approximate factor is proposed: $\sqrt{(\sqrt{\gamma_T} + 2)/3}$. The radii in the PRF divided by
34 the proposed scaling factor are falling on the common curve, therefore the scaling
35 can be recovered using the proposed scaling factor. The experimental analysis is
36 usually performed in the PRF (requires less statistics), hence the method of scal-
37 ing recovery enables easier testing of the hydrodynamic predictions, which are
38 not visible in the PRF.

Streszczenie

40 W tej pracy zaprezentowane są wyniki analizy dwucząstkowych korelacji pę-
41 dowych dla trzech różnych typów cząstek produkowanych w zderzeniach cięż-
42 kich jonów. Obliczenia zostały wykonane dla danych ze zderzeń ołów-ołów przy
43 energii w centrum masy $\sqrt{s_{NN}} = 2.76$ TeV wygenerowanych za pomocą mo-
44 delu THERMINATOR przy użyciu (3+1)-wymiarowego modelu hydrodynamicz-
45 nego uwzględniającego lepkość ośrodka. Analiza została wykonana dla trzech
46 rodzajów cząstek: pionów, kaonów i protonów dla dziewięciu różnych przedzia-
47 łów centralności.

48 Model THERMINATOR pozwala na wykonanie statystycznej hadronizacji
49 stabilnych cząstek jak i również niestabilnych rezonansów z danej
50 hiperpowierzchni wymrażania oraz uwzględnienie propagacji i rozpadów
51 tych rezonansów. Czterowymiarowa hiperpowierzchnia pochodzi z
52 obliczeń przeprowadzonych na podstawie hydrodynamiki relatywistycznej z
53 uwzględnieniem poprawek pochodzących od lepkości.

54 Interferometria dwucząstkowa pozwala na zbadanie charakterystyk
55 czasowo-przestrzennych źródła cząstek. Poprzez analizę danych pochodzących
56 z obliczeń modelowych można dokonać sprawdzenia zakresu stosownalności
57 hydrodynamiki do opisu właściwości plazmy kwarkowo-gluonowej. Ta praca
58 koncentruje się na weryfikacji skalowania promieni femtoskopowych z masą
59 poprzeczną przewidywanego przez hydrodynamikę.

60 Trójwymiarowe funkcje korelacyjne zostały obliczone za pomocą rozkładu w
61 szeregu harmonik sferycznych. To podejście wymaga mniejszej statystyki i po-
62 zwala na łatwiejszą wizualizację wyników. Obliczone funkcje korelacyjne wy-
63 kazują oczekiwany wzrost korelacji dla niskich różnic pędów dla par pionów i
64 kaonów. Dla par protonów w tym samym zakresie pędów widoczny jest spa-
65 dek korelacji. Widoczny jest wpływ pędu poprzecznego pary oraz centralności
66 na funkcję korelacyjną. W celu wykonania analizy ilościowej tego wpływu, zo-
67 stało wykonane dopasowanie formuły analitycznej do obliczonych funkcji kore-
68 lacyjnych. Otrzymane w ten sposób promienie femtoskopowe w LCMS i PRF
69 wykazują spadek wraz z wzrostem masy poprzecznej m_T . W celu sprawdzenie
70 skalowania przewidywanego przez hydrodynamikę została dopasowana zależ-
71 ność potęgowa: $\alpha m_T^{-\beta}$. Promienie obliczone dla pionów, kaonów i protonów
72 zachowują wzajemne skalowanie w LCMS. W przypadku PRF skalowanie nie
73 jest widoczne. Aby odzyskać skalowanie w PRF, został zaproponowany przy-
74 bliżony współczynnik: $\sqrt{(\sqrt{\gamma_T} + 2)/3}$. Promienie w PRF po podzieleniu przez

⁷⁵ współczynnik skalowania, są opisywalne przez podaną zależność potęgową, za-
⁷⁶ tem umożliwia on odzyskanie skalowania. Analiza eksperimentalna jest zazwy-
⁷⁷ czaj wykonywana w PRF (wymaga mniejszej statystyki), zatem ta metoda po-
⁷⁸ zwala na łatwiejszą weryfikację przewidywań hydrodynamiki które są widoczne
⁷⁹ w LCMS, a nie są w PRF.

⁸⁰ Contents

⁸¹	Introduction	1
⁸²	1 Theory of heavy ion collisions	3
⁸³	1.1 The Standard Model	3
⁸⁴	1.2 Quantum Chromodynamics	4
⁸⁵	1.2.1 Quarks and gluons	4
⁸⁶	1.2.2 Quantum Chromodynamics potential	5
⁸⁷	1.2.3 The quark-gluon plasma	7
⁸⁸	1.3 Relativistic heavy ion collisions	9
⁸⁹	1.3.1 Stages of heavy ion collision	9
⁹⁰	1.3.2 QGP signatures	11
⁹¹	2 Therminator model	19
⁹²	2.1 (3+1)-dimensional viscous hydrodynamics	19
⁹³	2.2 Statistical hadronization	20
⁹⁴	2.2.1 Cooper-Frye formalism	21
⁹⁵	2.3 Events generation procedure	22
⁹⁶	3 Particle interferometry	25
⁹⁷	3.1 HBT interferometry	25
⁹⁸	3.2 Theoretical approach	25
⁹⁹	3.2.1 Conventions used	26
¹⁰⁰	3.2.2 Two particle wave function	27
¹⁰¹	3.2.3 Source emission function	28
¹⁰²	3.2.4 Analytical form of a correlation function	30
¹⁰³	3.2.5 Spherical harmonics decomposition of a correlation function	31
¹⁰⁴	3.3 Experimental approach	32
¹⁰⁵	3.4 Scaling of femtoscopic radii	33
¹⁰⁶	3.4.1 Scaling in LCMS	34
¹⁰⁷	3.4.2 Scaling in PRF	35
¹⁰⁸	4 Results	36
¹⁰⁹	4.1 Identical particles correlations	36
¹¹⁰	4.1.1 Spherical harmonics components	36

111	4.1.2	Centrality dependence of a correlation function	40
112	4.1.3	k_T dependence of a correlation function	41
113	4.2	Results of the fitting procedure	42
114	4.2.1	The three-dimensional femtoscopic radii scaling	42
115	4.2.2	Scaling of one-dimensional radii	46
116	4.3	Discussion of the results	47
117	Conclusions		48
118	A	Scripts for events generation	50
119	B	Macros for fitting	52
120	C	Plotting scripts	53

¹²¹ Introduction

¹²² Many people were trying to discover what was in the beginning of the uni-
¹²³ verse which we observe today. Through the years, more or less successful theo-
¹²⁴ ries were appearing and trying to describe its origin and behaviour. Among them
¹²⁵ is one model, which provides a comprehensive explanation for a broad range
¹²⁶ of phenomena, including the cosmic microwave background, abundance of the
¹²⁷ light elements and Hubble's law. This model is called The Big Bang theory and
¹²⁸ has been born in 1927 on the basis of principles proposed by the Belgian priest and
¹²⁹ scientist Georges Lemaître. Using this model and known laws of physics one can
¹³⁰ calculate the characteristics of the universe in detail back in time to the extreme
¹³¹ densities and temperatures. However, at some point these calculations fail. The
¹³² extrapolation of the expansion of universe backwards in time using general re-
¹³³ lativity yields an infinite density and temperature at a finite time in the past. This
¹³⁴ appearance of singularity is a signal of the breakdown of general relativity. The
¹³⁵ range of this extrapolation towards singularity is debated - certainly we can go no
¹³⁶ closer than the end of *Planck epoch* i.e. 10^{-43} s. At this very first era the temperat-
¹³⁷ ure of the universe was so high, that the four fundamental forces - electromagnet-
¹³⁸ ism, gravitation, weak nuclear interaction and strong nuclear interaction - were
¹³⁹ one fundamental force. Between 10^{-43} s and 10^{-36} s of a lifetime of the universe,
¹⁴⁰ there is a *grand unification epoch*, at which forces are starting to separate from each
¹⁴¹ other. The *electroweak epoch* lasted from 10^{-36} s to 10^{-12} s, when the strong force
¹⁴² separated from the electroweak force. After the electroweak epoch, there was
¹⁴³ the *quark epoch* in which the universe was a dense "soup" of quarks. During this
¹⁴⁴ stage the fundamental forces of gravitation, electromagnetism, strong and weak
¹⁴⁵ interactions had taken their present forms. The temperature at this moment was
¹⁴⁶ still too high to allow quarks to bind together and form hadrons. At the end of
¹⁴⁷ quark era, there was a big freeze-out - when the average energy of particle inter-
¹⁴⁸ actions had fallen below the binding energy of hadrons. This era in which quarks
¹⁴⁹ became confined into hadrons is known as the hadron epoch. At this moment the
¹⁵⁰ matter had started forming nuclei and atoms, which we observe today.

¹⁵¹ Here arises the question: how can we study the very beginning of the
¹⁵² universe? To do this, one should create in a laboratory a system with such a
¹⁵³ large density and high temperature to recreate those conditions. Today, this is
¹⁵⁴ achievable through sophisticated machines, which are particle accelerators. In
¹⁵⁵ the particle accelerators, like the Large Hadron Collider at CERN, Geneva or

156 Relativistic Heavy Ion Collider at Brookhaven National Laboratory in Upton,
157 New York, the heavy ions after being accelerated to near the speed of light are
158 collided in order to generate extremely dense and hot phase of matter and
159 recreate the quark-gluon plasma. The plasma is believed to behave like an
160 almost ideal fluid and to become a medium, that can be described by the laws of
161 relativistic hydrodynamics.

162 This thesis is providing predictions for collective behaviour of the quark-
163 gluon plasma coming from the hydrodynamic equations. Experimental-like
164 analysis was performed for the high energy Pb-Pb collisions generated with
165 THERMINATOR model.

166 The 1st chapter is an introduction to the theory of heavy ion collisions. It
167 contains the brief description of the Standard Model and Quantum Chromody-
168 namics. The quark-gluon plasma and its signatures are also characterized.

169 In the 2nd chapter there is a description of the relativistic hydrodynamic
170 framework and the THERMINATOR model used to perform the simulations of col-
171 lisions.

172 The 3rd chapter covers the particle interferometry method used in this work.
173 The algorithm of building experimental correlation functions and effects coming
174 from the hydrodynamics in the experimental results for particle interferometry
175 are also presented.

176 In the 4th chapter there is a detailed analysis of the results for two-particle
177 femtoscopy for different pairs of particles. The quantitative analysis of calcu-
178 lated femtoscopic radii as well as the appearance of transverse mass scaling is
179 discussed.

¹⁸⁰ **Chapter 1**

¹⁸¹ **Theory of heavy ion collisions**

¹⁸² **1.1 The Standard Model**

¹⁸³ In the 1970s, a new theory of fundamental particles and their interaction
¹⁸⁴ emerged. It was a new concept, which combines the electromagnetic, weak and
¹⁸⁵ strong nuclear interactions between known particles. This theory is called *The*
¹⁸⁶ *Standard Model*. There are seventeen named particles in the standard model, or-
¹⁸⁷ ganized into the chart shown below (Fig. 1.1). Fundamental particles are divided
into two families: *fermions* and *bosons*.

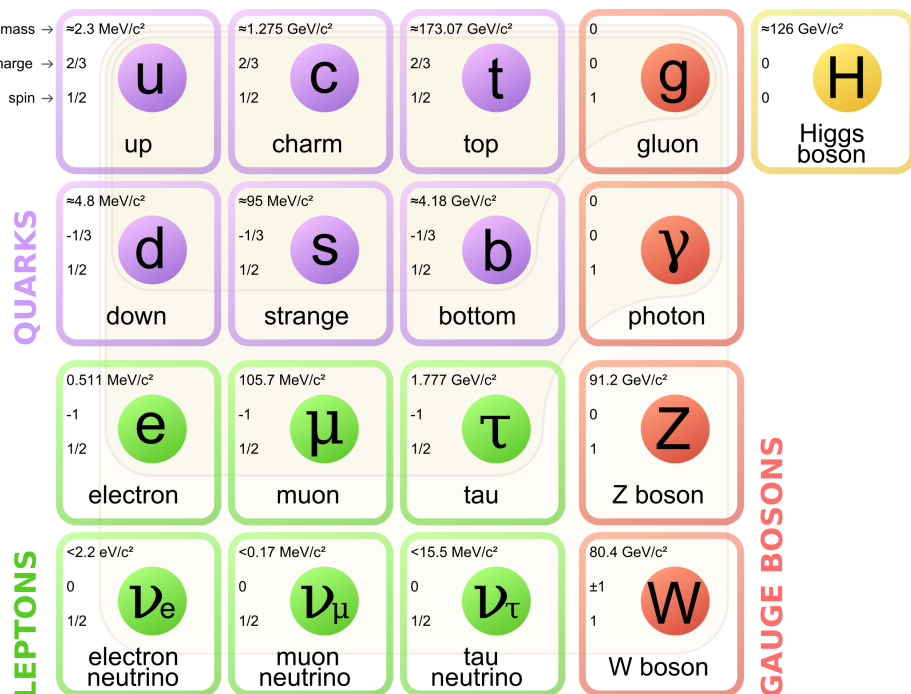


Figure 1.1: The Standard Model of elementary particles [1].

188 Fermions are the building blocks of matter. They are divided into two groups.
 189 Six of them, which must bind together are called *quarks*. Quarks are known to
 190 bind into doublets (*mesons*), triplets (*baryons*) and recently confirmed four-quark
 191 states.¹ Two of baryons, with the longest lifetimes, are forming a nucleus: a pro-
 192 ton and a neutron. A proton is build from two up quarks and one down, and
 193 neutron consists of two down quarks and one up. A proton is found to be a stable
 194 particle (at least it has a lifetime larger than 10^{35} years) and a free neutron has a
 195 mean lifetime about 8.8×10^2 s. Fermions, that can exist independently are called
 196 *leptons*. Neutrinos are a subgroup of leptons, which are only influenced by weak
 197 interaction. Fermions can be divided into three generations (three columns in
 198 the Figure 1.1). Generation I particles can combine into hadrons with the longest
 199 life spans. Generation II and III consists of unstable particles which also form
 200 unstable hadrons.

201 Bosons are force carriers. There are four fundamental forces: weak - respons-
 202ible for radioactive decay, strong - coupling quarks into hadrons, electromagnetic
 203 - between charged particles and gravity - the weakest, which causes the attraction
 204 between particles with mass. The Standard Model describes the first three. The
 205 weak force is mediated by W^\pm and Z^0 bosons, electromagnetic force is carried by
 206 photons γ and the carriers of a strong interaction are gluons g . The fifth boson is
 207 a Higgs boson which is responsible for giving other particles mass.

208 1.2 Quantum Chromodynamics

209 1.2.1 Quarks and gluons

210 Quarks interact with each other through the strong interaction. The medi-
 211 ator of this force is a *gluon* - a massless and electrical chargeless particle. In the
 212 quantum chromodynamics (QCD) - theory describing strong interaction - there
 213 are six types of "charges" (like electrical charges in the electrodynamics) called
 214 *colours*. The colours were introduced because some of the observed particles, like
 215 Δ^- , Δ^{++} and Ω^- appeared to consist of three quarks with the same flavour (*ddd*,
 216 *uuu* and *sss* respectively), which was in conflict with the Pauli principle. One
 217 quark can carry one of the three colours (usually called *red*, *green* and *blue*) and anti-
 218 quark one of the three anti-colours respectively. Only colour-neutral (or white)
 219 particles could exist. Mesons are assumed to be a colour-anticolour pair, while
 220 baryons are *red-green-blue* triplets. Gluons also are colour-charged and there are
 221 8 types of gluons. Therefore they can interact with themselves [3].

¹The LHCb experiment at CERN in Geneva confirmed recently the existence of $Z(4430)$ - a particle consisting of four quarks [2].

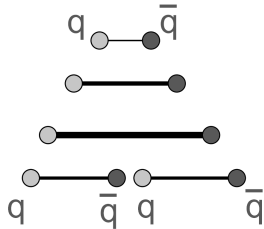
222 1.2.2 Quantum Chromodynamics potential

223 As a result of the fact that gluons are massless, one can expect, that the static
 224 potential in QCD will have the form like similar one in electrodynamics e.g.
 225 $\sim 1/r$ (by analogy to photons). In reality the QCD potential is assumed to have
 226 the form of [3]

$$227 V_s = -\frac{4}{3} \frac{\alpha_s}{r} + kr, \quad (1.1)$$

227 where the α_s is a coupling constant of the strong force and the kr part is related
 228 with *confinement*. In comparison to the electromagnetic force, a value of the strong
 229 coupling constant is $\alpha_s \approx 1$ and the electromagnetic one is $\alpha = 1/137$.

230 The fact that quarks does not exist separately and are always bound, is called
 231 confinement. As two quarks are pulled apart, the linear part kr in the Eq. 1.1
 232 becomes dominant and the potential becomes proportional to the distance. This
 233 situation resembles stretching of a string. At some point, when the string is so
 234 large it is energetically favourable to create a quark-antiquark pair. At this
 235 moment such pair (or pairs) is formed, the string breaks and the confinement is
 preserved (Fig. 1.2).



236 Figure 1.2: A string breaking and a creation of a new quark-antiquark pair [4].

237 On the other hand, for small r , an interaction between the quarks and gluons
 238 is dominated by the Coulomb-like term $-\frac{4}{3} \frac{\alpha_s}{r}$. The coupling constant α_s depends
 239 on the four-momentum Q^2 transferred in the interaction. This dependence is
 240 presented in Fig. 1.3. The value α_s decreases with increasing momentum trans-
 241 fer and the interaction becomes weak for large Q^2 , i.e. $\alpha_s(Q) \rightarrow 0$. Because
 242 of the weakening of coupling constant, quarks at large energies (or small dis-
 243 tances) are starting to behave like free particles. This phenomenon is known as
 244 *asymptotic freedom*. The QCD potential also has temperature dependence - the
 245 force strength "melts" with the temperature increase. Therefore the asymptotic
 246 freedom is expected to appear in either the case of high baryon densities (small
 247 distances between quarks) or very high temperatures. This temperature depend-
 248 ence is illustrated in Fig. 1.4.

249 If the coupling constant α_s is small, one can use perturbative methods to cal-
 250 culate physical observables. Perturbative QCD (pQCD) successfully describes
 251 hard processes (with large Q^2), such as jet production in high energy proton-
 252 antiproton collisions. The applicability of pQCD is defined by the *scale parameter*



Figure 1.3: The coupling parameter α_s dependence on four-momentum transfer Q^2 [5].

253 $\Lambda_{QCD} \approx 200$ MeV. If $Q \gg \Lambda_{QCD}$ then the process is in the perturbative domain
 254 and can be described by pQCD. A description of soft processes (when $Q < 1$ GeV)
 255 is a problem in QCD - perturbative theory breaks down at this scale. Therefore,
 256 to describe processes with low Q^2 , one has to use alternative methods like Lattice
 257 QCD. Lattice QCD (LQCD) is non-perturbative implementation of a field theory
 258 in which QCD quantities are calculated on a discrete space-time grid. LQCD al-
 259 lows to obtain properties of matter in equilibrium, but there are some limitations.
 260 Lattice QCD requires fine lattice spacing to obtain precise results - therefore large
 261 computational resources are necessary. With the constant growth of computing
 262 power this problem will become less important. The second problem is that lat-
 263 tice simulations are possible only for baryon density $\mu_B = 0$. At $\mu_B \neq 0$, Lattice
 264 QCD breaks down because of the sign problem. In QCD the thermodynamic
 265 observables are related to the grand canonical partition function, which has a ba-
 266 ryonic chemical potential μ_B as a parameter. Therefore, the baryonic density can
 267 be controlled by tuning the baryonic chemical potential. For fermions μ_B can be
 268 both positive and negative. For a particles with μ_B , their antiparticles have chem-
 269 ical potentials with opposite sign $-\mu_B$. Since at the early universe the number of
 270 baryons and antibaryons were almost equal we can use $\mu_B = 0$ to a very good
 271 approximation [6].

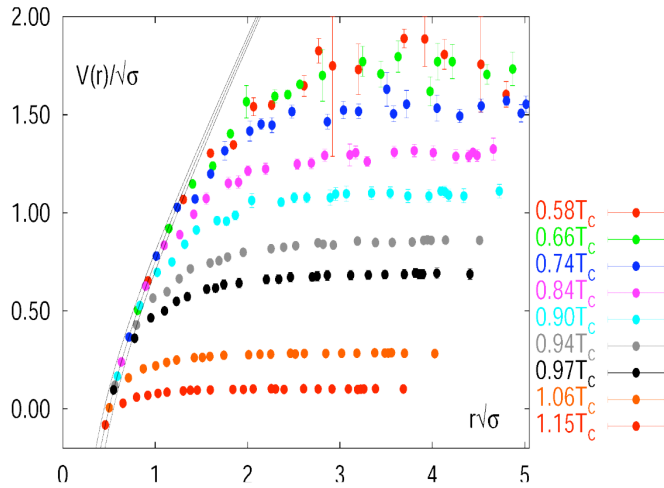


Figure 1.4: The QCD potential for a quark-antiquark pair as a function of distance for different temperatures. A value of a potential decreases with the temperature [4].

272 1.2.3 The quark-gluon plasma

273 The new state of matter in which quarks are no longer confined is known as
 274 a *quark-gluon plasma* (QGP). The predictions coming from the discrete space-time
 275 Lattice QCD calculations reveal a phase transition from the hadronic matter to
 276 the quark-gluon plasma at the high temperatures and baryon densities. The res-
 277 ults obtained from such calculations are shown on Fig. 1.5. The energy density
 278 ϵ which is divided by T^4 is a measure of the number of degrees of freedom in

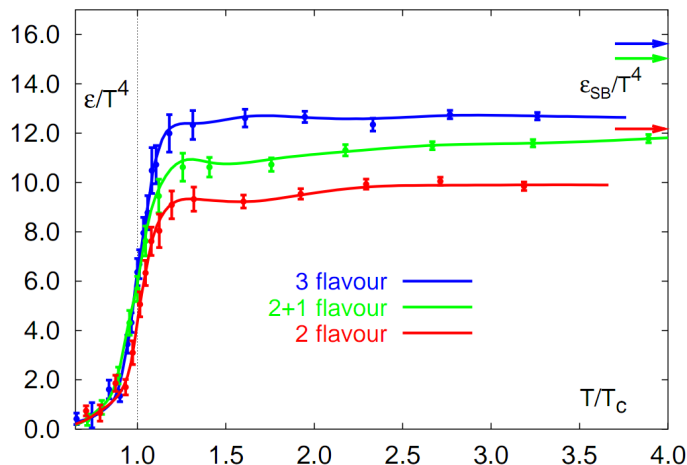


Figure 1.5: A number of degrees of freedom as a function of a temperature [7].

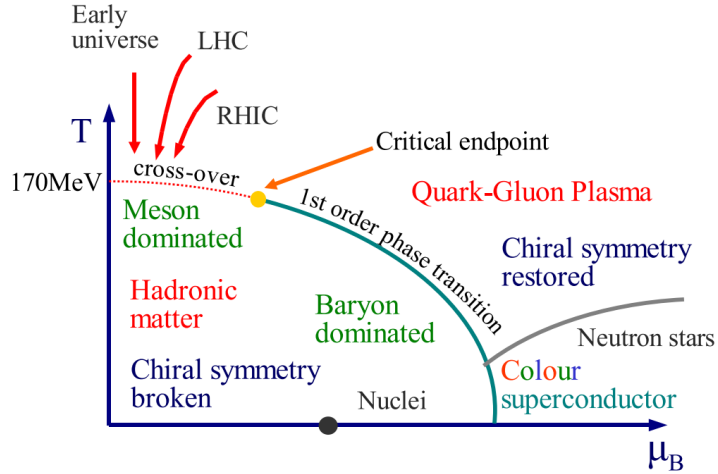


Figure 1.6: Phase diagram coming from the Lattice QCD calculations [8].

279 the system. One can observe significant rise of this value, when the temperature
 280 increases past the critical value T_C . Such increase is signaling a phase transition
 281 - the formation of QGP [8]. The values of the energy densities plotted in Fig. 1.5
 282 do not reach the Stefan-Boltzmann limit ϵ_{SB} (marked with arrows), which corre-
 283 sponds to an ideal gas. This can indicate some residual interactions in the system.
 284 According to the results from the RHIC², the new phase of matter behaves more
 285 like an ideal fluid, than like a gas [9].

286 One of the key questions, to which current heavy ion physics tries to find an
 287 answer is the value of a critical temperature T_C as a function of a baryon chem-
 288 ical potential μ_B (baryon density), where the phase transition occurs. The results
 289 coming from the Lattice QCD are presented in Fig. 1.6. The phase of matter in
 290 which quarks and gluons are deconfined is expected to exist at large temperat-
 291 ures. In the region of small temperatures and high baryon densities, a differ-
 292 ent state is supposed to appear - a *colour superconductor*. The phase transition
 293 between hadronic matter and the QGP is thought to be of 1st order at $\mu_B \gg 0$.
 294 However as $\mu_B \rightarrow 0$ quarks' masses become significant and a sharp transi-
 295 tion transforms into a rapid but smooth cross-over. It is believed that in Pb-Pb colli-
 296 sions observed at the LHC³, the created matter has high enough temperature to
 297 be in the quark-gluon plasma phase, then cools down and converts into hadrons,
 298 undergoing a smooth transition [8].

²Relativistic Heavy Ion Collider at Brookhaven National Laboratory in Upton, New York

³Large Hadron Collider at CERN, Geneva

299 1.3 Relativistic heavy ion collisions

300 1.3.1 Stages of heavy ion collision

301 To create the quark-gluon plasma one has to achieve high enough temper-
 302 atures and baryon densities. Such conditions can be recreated in the heavy ion
 303 collisions at the high energies. The left side of the Figure 1.7 shows simplified

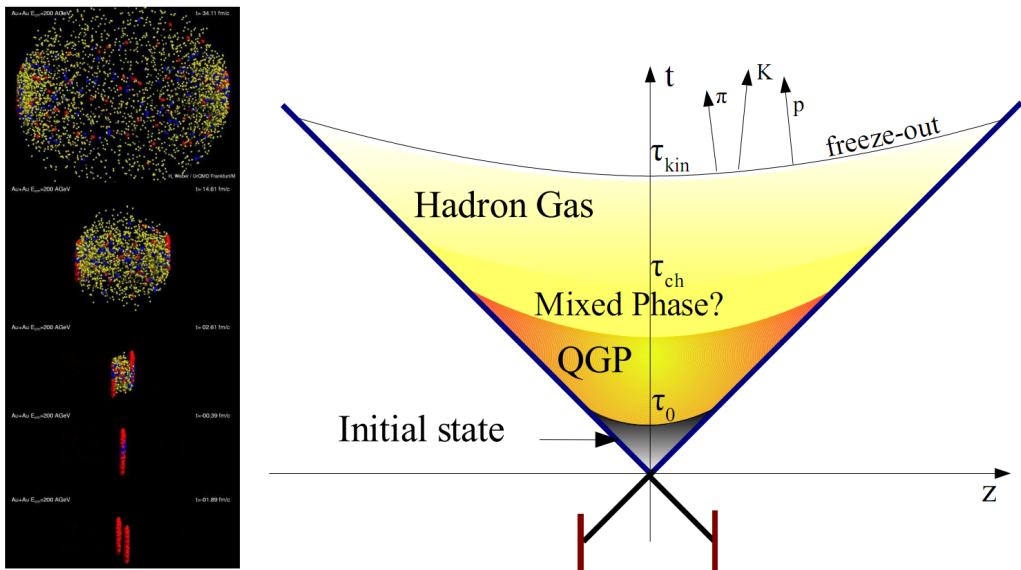


Figure 1.7: Left: stages of a heavy ion collision simulated in the UrQMD model.
 Right: schematic view of a heavy ion collision evolution [8].

303 picture of a central collision of two highly relativistic nuclei in the centre-of-
 304 mass reference frame. The colliding nuclei are presented as thin disks because
 305 of the Lorentz contraction. In the central region, where the energy density is the
 306 highest, a new state of matter - the quark-gluon plasma - is supposedly created.
 307 Afterwards, the plasma expands ad cools down, quarks combine into hadrons
 308 and their mutual interactions cease when the system reaches the *freeze-out* tem-
 309 perature. Subsequently, produced free hadrons move towards the detectors.
 310

311 On the right side of the Figure 1.7 a space-time evolution of a collision process
 312 is presented, plotted in the light-cone variables (z, t). The two highly relativistic
 313 nuclei are traveling basically along the light cone until they collide at the centre
 314 of the diagram. Nuclear fragments emerge from the collision again along the
 315 (forward) light cone, while the matter between fragmentation zones populates
 316 the central region. This hot and dense matter is believed to be in the state of the
 317 quark-gluon plasma. Several frameworks exist to describe this transition to the
 318 QGP phase, for example: QCD string breaking, QCD parton cascades or colour
 319 glass condensate evolving into glasma and later into quark-gluon plasma [10].

320 **String breaking** – In the string picture, the nuclei pass through each other forming colour strings. This is analogous to the situation depicted in the Fig 1.2 - the
 321 colour string is created between quarks inside particular nucleons in nuclei. In
 322 the next step strings decay / fragment forming quarks and gluons or directly
 323 hadrons. This approach becomes invalid at very high energies, when the strings
 324 overlap and cannot be treated as independent objects.

325 **Parton cascade** – The parton⁴ cascade model is based on the pQCD. The colliding
 326 nuclei are treated as clouds of quarks which penetrate through each other.
 327 The key element of this method is the time evolution of the parton phase-space
 328 distributions, which is governed by a relativistic Boltzmann equation with a col-
 329 lision term that contains dominant perturbative QCD interactions. The bottleneck
 330 of the parton cascade model is the low energies regime, where the Q^2 is too small
 331 to be described by the perturbative theory.

332 **Colour glass condensate** – The colour glass condensate assumes, that the had-
 333 ion can be viewed as a tightly packed system of interacting gluons. The sat-
 334 uration of gluons increases with energy, hence the total number of gluons may
 335 increase without bound. Such a saturated and weakly coupled gluon system is
 336 called a colour glass condensate. The fast gluons in the condensate are Lorentz
 337 contracted and redistributed on the two very thin sheets representing two col-
 338 liding nuclei. The sheets are perpendicular to the beam axis. The fast gluons
 339 produce mutually orthogonal colour magnetic and electric fields, that only ex-
 340 ist on the sheets. Immediately after the collision, i.e. just after the passage of
 341 the two gluonic sheets through each other, the longitudinal electric and magnetic
 342 fields are produced forming the *glasma*. The glasma fields decay through the
 343 classical rearrangement of the fields into radiation of gluons. Also decays due to
 344 the quantum pair creations are possible. In this way, the quark-gluon plasma is
 345 produced.

346 Interactions within the created quark-gluon plasma bring the system into
 347 the local statistical equilibrium, hence its further evolution can be described by
 348 the relativistic hydrodynamics. The hydrodynamic expansion causes the sys-
 349 tem to become more and more dilute. The phase transition from the quark-gluon
 350 plasma to the hadronic gas occurs. Further expansion causes a transition from the
 351 strongly interaction hadronic gas to weakly interacting system of hadrons which
 352 move freely to the detectors. Such decoupling of hadrons is called the *freeze-out*.
 353 The freeze-out can be divided into two phases: the chemical freeze-out and the
 354 thermal one. The *chemical freeze-out* occurs when the inelastic collisions between
 355 constituents of the hadron gas stop. As the system evolves from the chemical
 356 freeze-out to the thermal freeze-out the dominant processes are elastic collisions
 357 (such as, for example $\pi + \pi \rightarrow \rho \rightarrow \pi + \pi$) and strong decays of heavier reso-
 358 nances which populate the yield of stable hadrons. The *thermal freeze-out* is the
 359 stage of the evolution of matter, when the strongly coupled system transforms
 360 to a weakly coupled one (consisting of essentially free particles). In other words

⁴A parton is a common name for a quark and a gluon.

362 this is the moment, where the hadrons practically stop to interact. Obviously, the
 363 temperatures corresponding to the two freeze-outs satisfy the condition

$$T_{chem} > T_{therm}, \quad (1.2)$$

364 where T_{chem} (inferred from the ratios of hadron multiplicities) is the temperature
 365 of the chemical freeze-out, and T_{therm} (obtained from the investigation of the
 366 transverse-momentum spectra) is the temperature of the thermal freeze-out [10].

367 1.3.2 QGP signatures

368 The quark-gluon plasma is a very short living and unstable state of matter.
 369 One cannot investigate the properties of a plasma and confirm its existence directly.
 370 Hence, the several experimental effects were proposed as QGP signatures,
 371 some of them have been already observed in heavy ion experiments [8]. As matter
 372 created in the heavy ions collisions is supposed to behave like a fluid, one
 373 should expect appearance of collective behaviour at small transverse momenta
 374 - so called *elliptic flow* and *radial flow*. The next signal is the temperature range
 375 obtained from the measurements of *direct photons*, which gives us information,
 376 that the system created in heavy ion collisions is far above the critical temperat-
 377 ure obtained from the LQCD calculations. The *puzzle in the di-lepton spectrum* can
 378 be explained by the modification of spectral shape of vector mesons (mostly ρ
 379 meson) in the presence of a dense medium. This presence of a medium can also
 380 shed light on the *jet quenching* phenomenon - the suppression occurrence in the
 381 high p_T domain.

382 Elliptic flow

383 In a non-central heavy ion collisions, created region of matter has an almond
 384 shape with its shorter axis in the *reaction plane* (Fig. 1.8). The pressure gradient

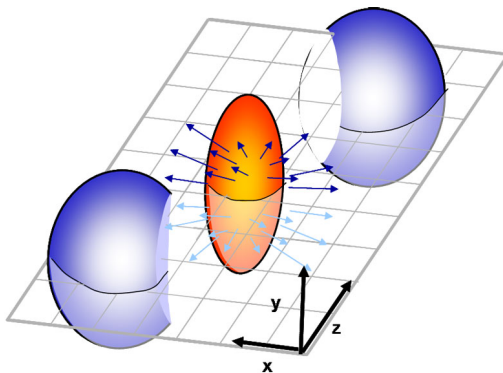


Figure 1.8: Overlapping region which is created in heavy ion collisions has an almond shape. Visible x-z plane is a *reaction plane*. The x-y plane is a *transverse plane*. The z is a direction of the beam [11].

is much larger in-plane rather than out-of-plane. This causes larger acceleration and transverse velocities in-plane rather than out-of-plane. Such differences can be investigated by studying the distribution of particles with respect to the reaction plane orientation [12]:

$$E \frac{d^3 N}{dp^3} = \frac{1}{2\pi} \frac{d^2 N}{p_T dp_T dy} (1 + 2v_1 \cos(\phi) + 2v_2 \cos(2\phi) + \dots), \quad (1.3)$$

where ϕ is the angle between particle transverse momentum p_T (a momentum projection on a transverse plane) and the reaction plane, N is a number of particles and E is an energy of a particle. The y variable is *rapidity* defined as:

$$y = \frac{1}{2} \ln \left(\frac{E + p_L}{E - p_L} \right), \quad (1.4)$$

where p_L is a longitudinal component of a momentum (parallel to the beam direction). The v_n coefficients indicate the shape of a system. For the most central collisions ($b = 0$ - see Fig. 1.9) all coefficients vanish $\sum_{n \in N_+} v_n = 0$ (the overlapping region has the spherical shape). The Fourier series elements in the parentheses in Eq. 1.3 represent different kinds of flow. The first value: "1" represents the *radial flow* - an isotropic flow in every direction. Next coefficient v_1 is responsible for *direct flow*. The v_2 coefficient is a measure of elliptic anisotropy (*elliptic flow*). The v_2 has to build up in the early stage of a collision - later the system becomes too dilute: space asymmetry and the pressure gradient vanish. Therefore the observation of elliptic flow means that the created matter was in fact a strongly interacting matter.

The v_2 coefficient was measured already at CERN SPS, LHC and RHIC. For the first time hydrodynamics successfully described the collision dynamics as the

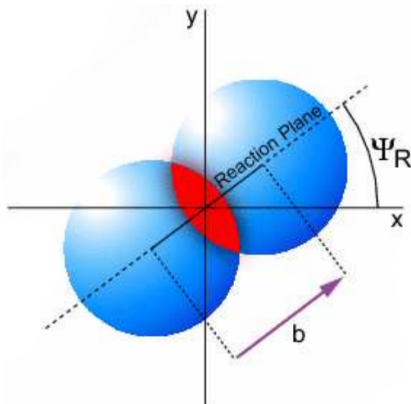


Figure 1.9: Cross-section of a heavy ion collision in a transverse plane. The b parameter is an *impact parameter* - a distance between centers of nuclei during a collision. An impact parameter is related with the centrality of a collision and a volume of the quark-gluon plasma [12].

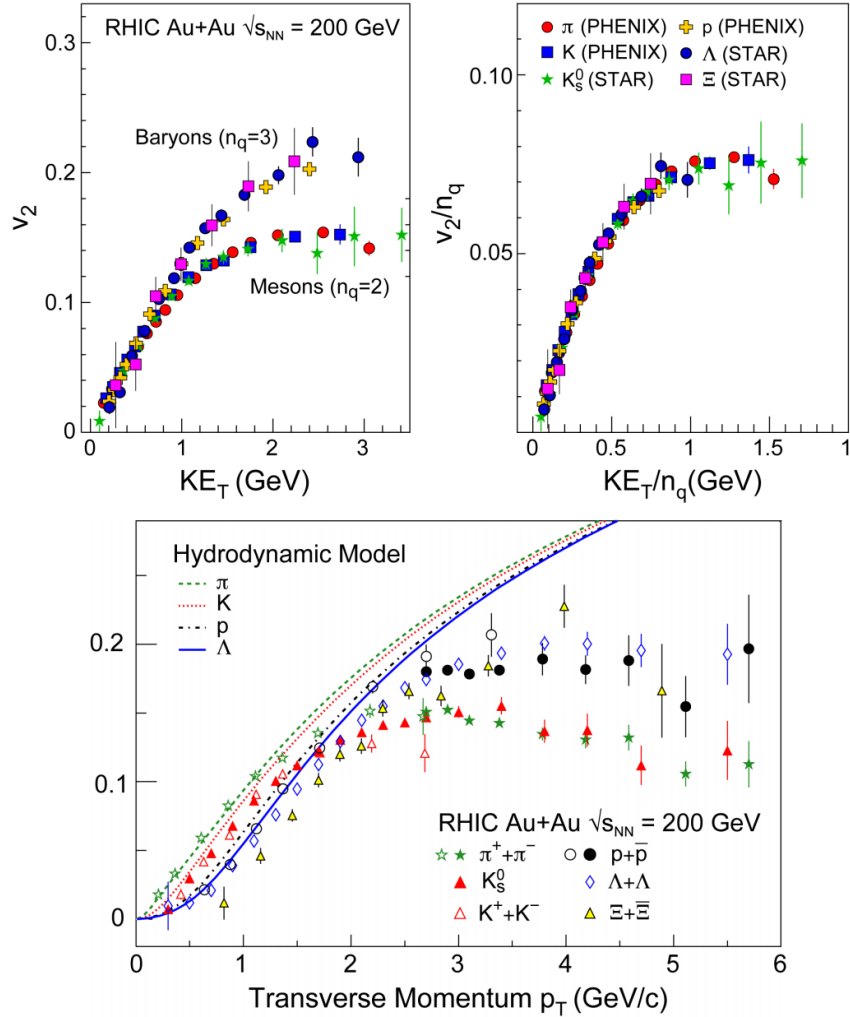


Figure 1.10: *Lower:* The elliptic flow v_2 follows the hydrodynamical predictions for an ideal fluid perfectly. Note that > 99% of all final hadrons have $p_T < 1.5 \text{ GeV}/c$. *Upper left:* The v_2 plotted versus transverse kinetic energy $KE_T = m_T - m_0 = \sqrt{p_T^2 + m_0^2} - m_0$. The v_2 follows different universal curves for mesons and baryons. *Upper right:* When scaled by the number of valence quarks, the v_2 follows the same universal curve for all hadrons and for all values of scaled transverse kinetic energy [13].

measured v_2 reached hydrodynamic limit (Fig. 1.10). As expected, there is a mass ordering of v_2 as a function of p_T (lower plot in the Fig. 1.10) with pions having the largest and protons the smallest anisotropy. In the upper plots in the Fig. 1.10 there is a v_2 as a function of transverse kinetic energy. The left plot shows two universal trend lines for baryons and mesons. After the scaling of v_2 and the

410 kinetic energy by the number of valence quarks, all of the hadrons follow the
 411 same universal curve. Those plots show that strong collectivity is observed in
 412 heavy ion collisions.

413 **Transverse radial flow**

414 Elliptic flow described previously is caused by the pressure gradients which
 415 must also produce a more simple collective behaviour of matter - a movement
 416 inside-out, called radial flow. Particles are pushed to higher momenta and they
 417 move away from the center of the collision. A source not showing collective
 418 behaviour, like pp collisions, produces particle spectra that can be fitted by a
 419 power-law [8]:

$$\frac{1}{2\pi p_T} \frac{d^2 N}{dp_T d\eta} = C \left(1 + \frac{p_T}{p_0} \right)^{-n} . \quad (1.5)$$

420 The η variable is *pseudorapidity* defined as follows:

$$\eta = \frac{1}{2} \ln \left(\frac{p + p_L}{p - p_L} \right) = -\ln \left(\frac{\theta}{2} \right) , \quad (1.6)$$

where θ is an emission angle $\cos \theta = p_L/p$.

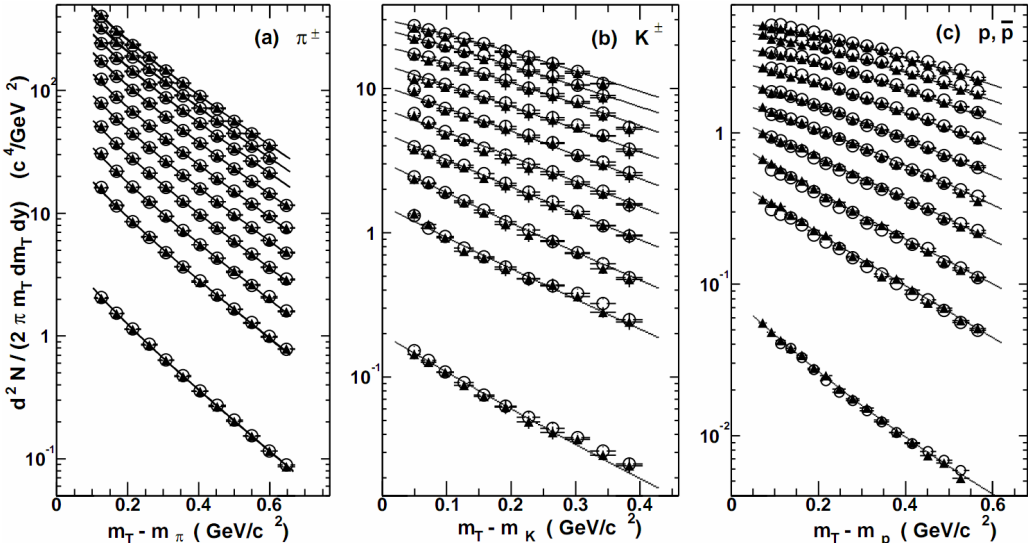


Figure 1.11: Invariant yield of particles versus transverse mass $m_T = \sqrt{p_T^2 + m_0^2}$ for π^\pm , K^\pm , p and \bar{p} at mid-rapidity for p+p collisions (bottom) and Au+Au events from 70-80% (second bottom) to 0-5% (top) centrality [14].

421
 422 The hydrodynamical expansion of a system gives the same flow velocity kick
 423 for different kinds of particles - ones with bigger masses will gain larger p_T boost.
 424 This causes increase of the yield of particles with larger transverse momenta. In

the invariant yield plots one can observe the decrease of the slope parameter, especially for the heavier hadrons. This is presented in the Fig. 1.11. The most affected spectra are ones of kaons (b) and protons (c). One can notice decrease of the slope parameter for heavy ion collisions (plots from second bottom to top) comparing to the proton-proton collisions (bottom ones), where no boost from radial flow should occur [8].

Another signature of a transverse radial flow is a dependence of HBT radii on a pair transverse momentum. Detailed description of this effect is presented in the Section 3.4.

434 Direct photons

The direct photons are photons, which are not coming from the final state hadrons decays. Their sources can be various interaction from charged particles created in the collision, either at the partonic or at the hadronic level. Direct photons are considered to be an excellent probe of the early stage of the collision. This is because their mean free path is very large when compared to the size of created system in the collision. Thus photons created at the early stage leave the system without suffering any interaction and retain information about this stage, in particular about its temperature.

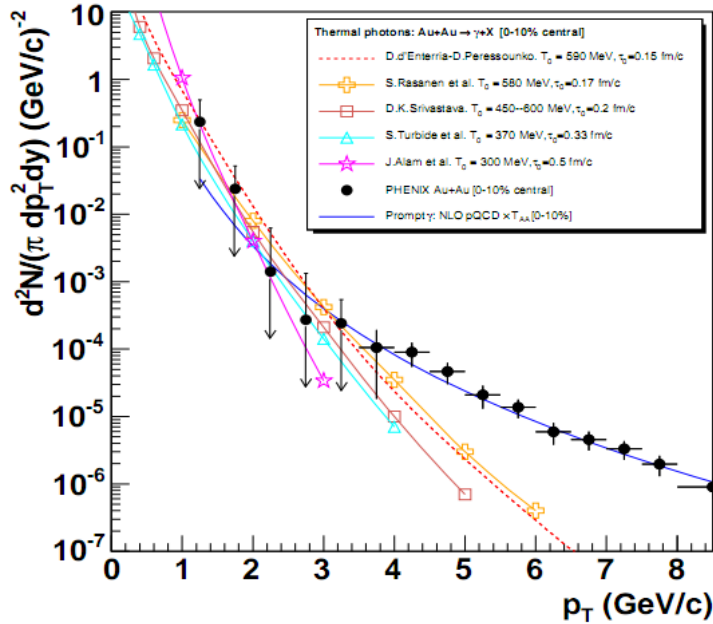


Figure 1.12: Thermal photons spectra for the central Au+Au collisions at $\sqrt{s_{NN}} = 200$ GeV computed within different hydrodynamical models compared with the pQCD calculations (solid line) and experimental data from PHENIX (black dots) [15].

One can distinguish two kinds of direct photons: *thermal* and *prompt*. Thermal photons can be emitted from the strong processes in the quark-gluon plasma involving quarks and gluons or hot hadronic matter (e.g. processes: $\pi\pi \rightarrow \rho\gamma$, $\pi\rho \rightarrow \pi\gamma$). Thermal photons can be observed in the low p_T region. Prompt photons are believed to come from “hard” collisions of initial state partons belonging to the colliding nuclei. The prompt photons can be described using the pQCD. They will dominate the high p_T region. The analysis of transverse momentum of spectra of direct photons revealed, that the temperature of the source of thermal photons produced in heavy ion collisions at RHIC is in the range 300–600 MeV (Fig. 1.12). Hence the direct photons had to come from a system whose temperature is far above from the critical temperature for QGP creation.

Puzzle in di-lepton mass spectrum

The invariant mass spectra (Fig. 1.13) of lepton pairs reveal many peaks corresponding to direct decays of various mesons into a lepton pair. The continuous background in this plot is caused by the decays of hadrons into more than two leptons (including so-called *Dalitz decays* into a lepton pair and a photon). Particular hadron decay channels, which contribute to this spectrum are shown

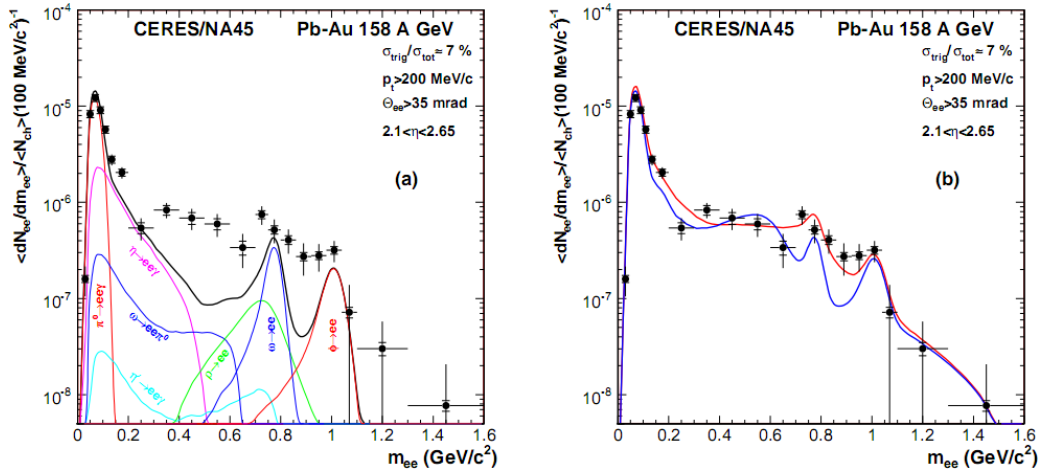


Figure 1.13: Left: Invariant mass spectrum of $e^+ - e^-$ pairs in $Pb+Au$ collisions at 158A GeV compared to the sum coming from the hadron decays predictions. Right: The expectations coming from model calculations assuming a dropping of the ρ mass (blue) or a spread of the ρ width in the medium (red) [16].

in Fig. 1.13 with the coloured lines and their sum with the black one. The sum (called *the hadronic cocktail*) of various components describes experimental spectra coming from the simple collisions (like $p+p$ or $p+A$) quite well with the statistical and systematical uncertainties [9]. This situation is different considering more complicated systems i.e. $A+A$. Spectra coming from $Pb+Au$ collisions are presented on the plots in the Fig. 1.13. The “hadronic cocktail” does not describe

the data, in the mass range between the π and the ρ mesons a significant excess of electron pairs over the calculated sum is observed. Theoretical explanation of this phenomenon assumes modification of the spectral shape of vector mesons in a dense medium. Two different interpretations of this increase were proposed: a decrease of meson mass with the medium density and increase of the meson width in the dense medium. In principle, one could think of simultaneous occurrence of both effects: mass shift and resonance broadening. Experimental results coming from the CERES disfavour the mass shift hypothesis indicating only broadening of resonance peaks (Fig. 1.13b) [9].

475 Jet quenching

A jet is defined as a group of particles with close vector momenta and high energies. It has its beginning when the two partons are going in opposite directions and have energy big enough to produce new quark-antiquark pair and then radiate gluons. This process can be repeated many times and it results in two back-to-back jets of hadrons. It has been found that jets in the opposite hemisphere (*away-side jets*) show a very different pattern in d+Au and Au+Au collisions. This is shown in the azimuthal correlations in the Fig. 1.14. In d+Au collisions, like in p+p, a pronounced away-side jet appears around $\Delta\phi = \pi$, exactly opposite to the trigger jet, which is typical for di-jet events. In central Au+Au collisions the away-side jet is suppressed. When the jet has its beginning near the surface of the quark-gluon plasma, one of the jets (*near-side jet*) leaves the system almost without any interactions. This jet is visible on the correlation plot as a high peak

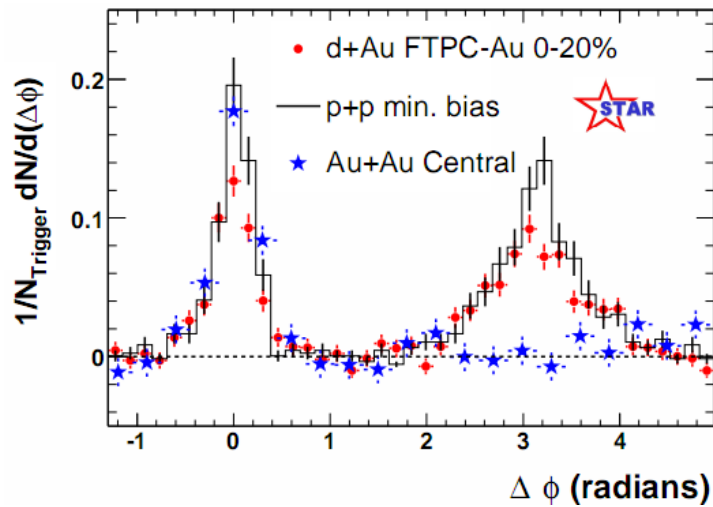


Figure 1.14: Azimuthal angle difference $\Delta\phi$ distributions for different colliding systems at $\sqrt{s_{NN}} = 200$ GeV. Transverse momentum cut: $p_T > 2$ GeV. For the Au+Au collisions the away-side jet is missing [17].

488 at $\Delta\phi = 0$. However, the jet moving towards the opposite direction has to penetrate
489 a dense medium. The interaction with the plasma causes energy dissipation
490 of particles and is visible on an azimuthal correlation plot as a disappearance of
491 the away-side jet [9].

492 **Chapter 2**

493 **Therminator model**

494 THERMINATOR [18] is a Monte Carlo event generator designed to investigate
495 the particle production in the relativistic heavy ion collisions. The functionality
496 of the code includes a generation of the stable particles and unstable resonances
497 at the chosen hypersurface model. It performs the statistical hadronization which
498 is followed by space-time evolution of particles and the decay of resonances. The
499 key element of this method is an inclusion of a complete list of hadronic reso-
500 nances, which contribute very significantly to the observables. The second version
501 of THERMINATOR [19] comes with a possibility to incorporate any shape of freeze-
502 out hypersurface and the expansion velocity field, especially those generated ex-
503 ternally with various hydrodynamic codes.

504 **2.1 (3+1)-dimensional viscous hydrodynamics**

505 Most of the relativistic viscous hydrodynamic calculations are done in
506 (2+1)-dimensions. Such simplification assumes boost-invariance of a matter
507 created in a collision. Experimental data reveals that no boost-invariant region is
508 formed in the collisions [20]. Hence, for the better description of created system
509 a (3+1)-dimensional model is required.

510 In the four dimensional relativistic dynamics one can describe a system
511 using a space-time four-vector $x^\nu = (ct, x, y, z)$, a velocity four-vector
512 $u^\nu = \gamma(c, v_x, v_y, v_z)$ and a energy-momentum tensor $T^{\mu\nu}$. The particular
513 components of $T^{\mu\nu}$ have a following meaning:

- 514 • T^{00} - an energy density,
- 515 • $cT^{0\alpha}$ - an energy flux across a surface x^α ,
- 516 • $T^{\alpha 0}$ - an α -momentum flux across a surface x^α multiplied by c ,
- 517 • $T^{\alpha\beta}$ - components of momentum flux density tensor,

518 where $\gamma = (1 - v^2/c^2)^{-1/2}$ is Lorentz factor and $\alpha, \beta \in \{1, 2, 3\}$. Using u^ν one can
 519 express $T^{\mu\nu}$ as follows [21]:

$$T_0^{\mu\nu} = (e + p)u^\mu u^\nu - pg^{\mu\nu} \quad (2.1)$$

520 where e is an energy density, p is a pressure and $g^{\mu\nu}$ is an inverse metric tensor:

$$g^{\mu\nu} = \begin{bmatrix} 1 & 0 & 0 & 0 \\ 0 & -1 & 0 & 0 \\ 0 & 0 & -1 & 0 \\ 0 & 0 & 0 & -1 \end{bmatrix}. \quad (2.2)$$

521 The presented version of energy-momentum tensor (Eq. 2.1) can be used to de-
 522 scribe dynamics of a perfect fluid. To take into account influence of viscosity,
 523 one has to apply the following corrections coming from shear $\pi^{\mu\nu}$ and bulk Π
 524 viscosities [22]:

$$T^{\mu\nu} = T_0^{\mu\nu} + \pi^{\mu\nu} + \Pi(g^{\mu\nu} - u^\mu u^\nu). \quad (2.3)$$

525 The stress tensor $\pi^{\mu\nu}$ and the bulk viscosity Π are solutions of dynamical equa-
 526 tions in the second order viscous hydrodynamic framework [21]. The compari-
 527 son of hydrodynamics calculations with the experimental results reveal, that the
 528 shear viscosity divided by entropy η/s has to be small and close to the AdS/CFT
 529 estimate $\eta/s = 0.08$ [22, 23]. The bulk viscosity over entropy value used in calcu-
 530 lations is $\zeta/s = 0.04$ [22].

531 When using $T^{\mu\nu}$ to describe system evolving close to local thermodynamic
 532 equilibrium, relativistic hydrodynamic equations in a form of:

$$\partial_\mu T^{\mu\nu} = 0 \quad (2.4)$$

533 can be used to describe the dynamics of the local energy density, pressure and
 534 flow velocity.

535 Hydrodynamic calculations are starting from the Glauber¹ model initial con-
 536 ditions. The collective expansion of a fluid ends at the freeze-out hypersurface.
 537 That surface is usually defined as a constant temperature surface, or equivalently
 538 as a cut-off in local energy density. The freeze-out is assumed to occur at the
 539 temperature $T = 140$ MeV.

540 2.2 Statistical hadronization

541 Statistical description of heavy ion collision has been successfully used to
 542 quantitatively describe the *soft* physics, i.e. the regime with the transverse mo-
 543 mentum not exceeding 2 GeV. The basic assumption of the statistical approach of
 544 evolution of the quark-gluon plasma is that at some point of the space-time evol-
 545 ution of the fireball, the thermal equilibrium is reached. When the system is in the

¹The Glauber Model is used to calculate “geometrical” parameters of a collision like an impact parameter, number of participating nucleons or number of binary collisions.

546 thermal equilibrium the local phase-space densities of particles follow the Fermi-
 547 Dirac or Bose-Einstein statistical distributions. At the end of the plasma expan-
 548 sion, the freeze-out occurs. The freeze-out model incorporated in THERMINATOR
 549 assumes, that chemical and thermal freeze-outs occur at the same time.

550 **2.2.1 Cooper-Frye formalism**

551 The result of the hydrodynamic calculations is the freeze-out hyper-
 552 surface Σ^μ . A three-dimensional element of the surface is defined as [19]

$$553 \quad d\Sigma_\mu = \epsilon_{\mu\alpha\beta\gamma} \frac{\partial x^\alpha}{\partial \alpha} \frac{\partial x^\beta}{\partial \beta} \frac{\partial x^\gamma}{\partial \gamma} d\alpha d\beta d\gamma, \quad (2.5)$$

554 where $\epsilon_{\mu\alpha\beta\gamma}$ is the Levi-Civita tensor and the variables $\alpha, \beta, \gamma \in \{1, 2, 3\}$ are used
 555 to parametrize the three-dimensional freeze-out hypersurface in the Minkowski
 556 four-dimensional space. The Levi-Civita tensor is equal to 1 when the indices
 557 form an even permutation (eg. ϵ_{0123}), to -1 when the permutation is odd (e.g.
 558 ϵ_{2134}) and has a value of 0 if any index is repeated. Therefore [19],

$$559 \quad d\Sigma_0 = \begin{vmatrix} \frac{\partial x}{\partial \alpha} & \frac{\partial x}{\partial \beta} & \frac{\partial x}{\partial \gamma} \\ \frac{\partial y}{\partial \alpha} & \frac{\partial y}{\partial \beta} & \frac{\partial y}{\partial \gamma} \\ \frac{\partial z}{\partial \alpha} & \frac{\partial z}{\partial \beta} & \frac{\partial z}{\partial \gamma} \end{vmatrix} d\alpha d\beta d\gamma \quad (2.6)$$

560 and the remaining components are obtained by cyclic permutations of t, x, y
 561 and z .

One can obtain the number of hadrons produced on the hypersurface Σ^μ from
 the Cooper-Frye formalism. The following integral yields the total number of
 created particles [19]:

$$562 \quad N = (2s + 1) \int \frac{d^3 p}{(2\pi)^3 E_p} \int d\Sigma_\mu p^\mu f(p_\mu u^\mu), \quad (2.7)$$

563 where $f(p_\mu u^\mu)$ is the phase-space distribution of particles (for stable ones and res-
 564 onances). One can simply derive from Eq. 2.7, the dependence of the momentum
 565 density [24]:

$$566 \quad E \frac{d^3 N}{dp^3} = \int d\Sigma_\mu f(p_\mu u^\mu) p^\mu. \quad (2.8)$$

567 The momentum distribution f contains non-equilibrium corrections:

$$568 \quad f = f_0 + \delta f_{shear} + \delta f_{bulk}, \quad (2.9)$$

569 where

$$570 \quad f_0(p_\mu u^\mu) = \left\{ \exp \left[\frac{p_\mu u^\mu - (B\mu_B + I_3\mu_{I_3} + S\mu_S + C\mu_C)}{T} \right] \pm 1 \right\}^{-1}. \quad (2.10)$$

566 In case of fermions, in the Eq. 2.10 there is a plus sign and for bosons, minus
 567 sign respectively. The thermodynamic quantities appearing in the $f_0(\cdot)$ are T -
 568 temperature, μ_B - baryon chemical potential, μ_{I_3} - isospin chemical potential, μ_S
 569 - strange chemical potential, μ_C - charmed chemical potential and the s is a spin of
 570 a particle. The hydrodynamic calculations yield the flow velocity at freeze-out as
 571 well as the stress and bulk viscosity tensors required to calculate non-equilibrium
 572 corrections to the momentum distribution used in Eq. 2.7. The term coming from
 573 shear viscosity has a form [22]

$$\delta f_{shear} = f_0(1 \pm f_0) \frac{1}{2T^2(e + p)} p^\mu p^\nu \pi_{\mu\nu} \quad (2.11)$$

574 and bulk viscosity

$$\delta f_{bulk} = C f_0(1 \pm f_0) \left(\frac{(u^\mu p_\mu)^2}{3u^\mu p_\mu} - c_s^2 u^\mu p_\mu \right) \Pi \quad (2.12)$$

575 where c_s is sound velocity and

$$\frac{1}{C} = \frac{1}{3} \frac{1}{(2\pi)^3} \sum_{hadrons} \int d^3 p \frac{m^2}{E} f_0(1 \pm f_0) \left(\frac{p^2}{3E} - c_s^2 E \right). \quad (2.13)$$

576 2.3 Events generation procedure

577 The equations presented in the previous section are directly used in the
 578 THERMINATOR to generate the primordial hadrons (created during freeze-out)
 579 with the Monte-Carlo method. This procedure consists of 3 main steps, where
 580 the first two are performed only once per given parameter set. After the
 581 generation of primordial particles, the cascade decay of unstable resonances is
 582 performed.

583 Determination of a maximum of an integrand

584 In order to generate particles through a Monte Carlo method, the maximum
 585 value of the distribution in the right-hand-side of Eq. 2.7 must be known. To find
 586 this number, THERMINATOR performs a generation of a sample consisting of a
 587 large number of particles. For each particle the value of a distribution is cal-
 588 culated and the maximum value f_{max} of the sample is stored. A large enough
 589 sample of particles guarantees that f_{max} found in this procedure is a good es-
 590 timate of the maximum value of a distribution in Eq. 2.7. This maximum value
 591 depends on a particle type and values of parameters, but does not change from
 592 event to event, hence this procedure is performed once, at the beginning of the
 593 events generation [18].

594 **Multiplicity calculation**

595 In order to generate events, a multiplicity of each particle must be known.
 596 The multiplicities are obtained through a numerical integration of distribution
 597 functions (Eq. 2.7) in the given integration ranges determined by the model para-
 598 meters. The multiplicities also depend only on the model parameters and they
 599 are also only calculated once at the beginning of the event generation [18].

600 **Events and particles generation**

601 Each of the events produced by THERMINATOR are generated separately. At
 602 first, the multiplicities for each of particle type are generated as random numbers
 603 from a Poisson distribution, with the mean being the average particle multipli-
 604 city determined in the previous step. Then the program proceeds to generate
 605 particles from the heaviest to the lightest particle type. In essence, this procedure
 606 is a generation of the set of six random numbers: three components of particle's
 607 momentum (p_x, p_y, p_z) and three parameters providing space-time coordinates
 608 on a freeze-out hypersurface (ζ, ϕ_s, θ). Event generation procedure is based on
 609 von Neumann's acceptance-rejection algorithm. Firstly, the integrand in Eq. 2.7
 610 is calculated using given set of numbers. Subsequently, a random number from
 611 uniform distribution over $[0; f_{max}]$ is compared to the value of integrand. If it
 612 is lower, then the set of numbers is stored as actual particle. If this condition
 613 was not satisfied, a new set is generated. This procedure is repeated until the
 614 determined number of particles of each kind is generated. At this point all prim-
 615 ordial particles (stable and resonances) have been generated and stored in the
 616 event [18].

617 **Decays of unstable particles**

618 In the next step of event generation, a simulation of decays of unstable res-
 619 onances is performed. A particle is considered as unstable when it has non-zero
 620 width Γ defined in the input files of THERMINATOR. The decays proceed sequen-
 621 tially from the heaviest particles to the lightest. Unstable products of decays are
 622 added to the particles generated in the current event and are processed in the
 623 subsequent steps. If a particle has several decay channels, one of them is selec-
 624 ted randomly with the appropriate probability corresponding to the branching
 625 ratio provided in the input files. THERMINATOR in the hadronic cascade process
 626 performs two-body and three-body decays.

627 At the beginning of the cascade decay, the lifetime τ of a particle with mass
 628 M , moving with the four-momentum p^μ , is generated randomly according to the
 629 exponential decay law $\exp(-\Gamma\tau)$. When the lifetime is known, the point of its
 630 decay is calculated as [18]:

$$x_{decay}^\mu = x_{origin}^\mu + \frac{p^\mu}{M}\tau, \quad (2.14)$$

631 where x_{origin}^μ is a space-time position, where the unstable particle was generated.
 632 At the x_{decay}^μ point decay occurs and daughter particles with energies and mo-
 633 ments determined by the conservation laws are generated. Fig. 2.1 illustrates the
 cascade decay process [18].

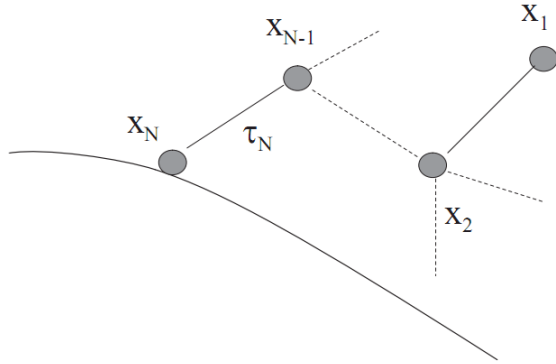


Figure 2.1: The cascade decay in the single freeze-out model. An unstable resonance x_N is formed at the freeze-out hypersurface and travels for the time τ_N depending on its lifetime and decays. If the products are also resonances (x_{N-1} , x_2) they decay further until the stable particles are formed (x_1) [18].

635 **Chapter 3**

636 **Particle interferometry**

637 Two-particle interferometry (also called *femtoscopy*) gives a possibility to
638 investigate space-time characteristics of the particle-emitting source created
639 in heavy ion collisions. Through the study of particle correlations, their
640 momentum distributions can be used to obtain information about the spatial
641 extent of the created system. Using this method, one can measure sizes of the
642 order of 10^{-15} m and time of the order of 10^{-23} s.

643 **3.1 HBT interferometry**

644 In the 1956 Robert Hanbury Brown and Richard Q. Twiss proposed a method
645 which allowed to investigate angular dimensions of stars through analysis of
646 interference between photons. They performed a measurement of the intensity
647 of a beam of light coming from a star using two separated detectors. In a sig-
648 nal plotted as a function of distance between detectors an interference effect was
649 observed, revealing a positive correlation, despite the fact that no phase inform-
650 ation was collected. Hanbury, Brown and Twiss used this interference signal to
651 calculate the angular size of a star with the excellent resolution. This method was
652 designed to be used in astronomy, however HBT interferometry can be used also
653 to measure extent of any emitting source. Therefore it was adapted to heavy ion
654 collisions to investigate dimensions of a particle-emitting source [8].

655 **3.2 Theoretical approach**

656 Intensity interferometry in heavy ion physics uses similar mathematical form-
657 alism as the astronomy HBT measurement. The difference between them is that
658 femtoscopy uses a two-particle relative momentum and yields the space-time
659 picture of a source, whereas the latter method uses the distance between detect-
660 ors to calculate angular size of the star.

661 **3.2.1 Conventions used**

662 In heavy ion collisions to describe particular directions, components of mo-
 663 mentum and location of particles, one uses naming convention called the Bertsch-
 Pratt coordinate system. This system is presented in the Fig. 3.1. The three dir-

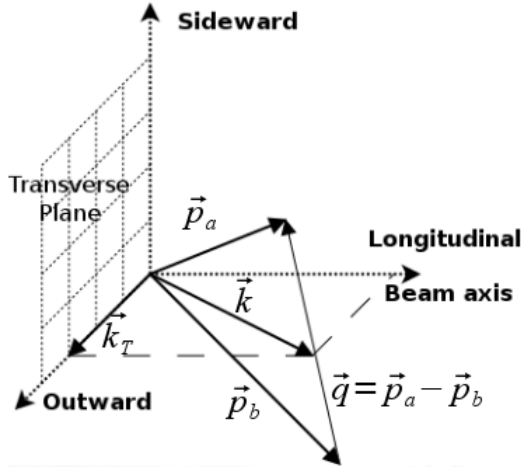


Figure 3.1: Bertsch-Pratt direction naming convention used in heavy ion collision.

664
 665 ections are called *longitudinal*, *outward* and *sideward*. The longitudinal direction
 666 is parallel to the beam axis. The plane perpendicular to the beam axis is called
 667 a *transverse plane*. A projection of a particle pair momentum $\mathbf{k} = (\mathbf{p}_a + \mathbf{p}_b)/2$
 668 on a transverse plane (a *transverse momentum* \mathbf{k}_T) determines *outward* direction:
 669 $(\mathbf{k})_{out} = \mathbf{k}_T$. A direction perpendicular to the longitudinal and outward is called
 670 *sideward*.

671 A particle pair is usually described using two coordinate systems. The first
 672 one, *Longitudinally Co-Moving System* (LCMS) is moving along the particle pair
 673 with the longitudinal direction, in other words, the pair longitudinal momentum
 674 vanishes: $(\mathbf{p}_a)_{long} = -(\mathbf{p}_b)_{long}$. The second system is called *Pair Rest Frame* (PRF).
 675 In the PRF the centre of mass rests: $\mathbf{p}_a = -\mathbf{p}_b$. Variables which are expressed in
 676 the PRF are marked with a star (e.g. \mathbf{k}^*).

The transition of space-time coordinates from LCMS to PRF is simply
 a boost along the outward direction, with the transverse velocity of the
 pair $\beta_T = (\mathbf{v}/c)_{out}$ [25]:

$$r_{out}^* = \gamma_t(r_{out} - \beta_T \Delta t) \quad (3.1)$$

$$r_{side}^* = r_{side} \quad (3.2)$$

$$r_{long}^* = r_{long} \quad (3.3)$$

$$\Delta t^* = \gamma_T(\Delta t - \beta_T r_{out}), \quad (3.4)$$

677 where $\gamma_T = (1 - \beta_T^2)^{-1/2}$ is the Lorentz factor. However, in calculations performed

in this work the equal time approximation is used, which assumes that particles in a pair were produced at the same time in PRF - the Δt^* is neglected.

The most important variables used to describe particle pair are their total momentum $\mathbf{P} = \mathbf{p}_a + \mathbf{p}_b$ and relative momentum $\mathbf{q} = \mathbf{p}_a - \mathbf{p}_b$. In the PRF one has $\mathbf{q} = 2\mathbf{k}^*$, where \mathbf{k}^* is a momentum of the first particle in PRF.

3.2.2 Two particle wave function

Let us consider two identical particles with momenta \mathbf{p}_1 and \mathbf{p}_2 emitted from space points \mathbf{x}_1 and \mathbf{x}_2 . Those emitted particles can be treated as two incoherent waves. If the particles are identical, they are also indistinguishable, therefore one

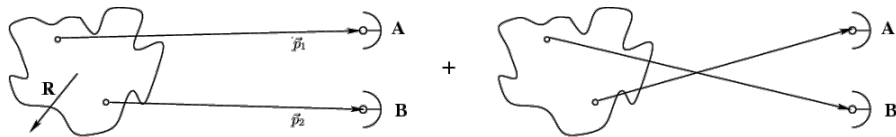


Figure 3.2: The pair wave function is a superposition of all possible states. In case of particle interferometry it includes two cases: particles with momenta p_1, p_2 registered by detectors A, B and p_1, p_2 registered by B, A respectively.

has also take into account the scenario, where the particle with momentum \mathbf{p}_1 is emitted from \mathbf{x}_2 and particle \mathbf{p}_2 from \mathbf{x}_1 (Fig. 3.2). In such case, the wave function describing behaviour of a pair has to contain both components [8]:

$$\Psi_{ab}(\mathbf{q}) = \frac{1}{\sqrt{2}} [\exp(-i\mathbf{p}_1\mathbf{x}_1 - i\mathbf{p}_2\mathbf{x}_2) \pm \exp(-i\mathbf{p}_2\mathbf{x}_1 - i\mathbf{p}_1\mathbf{x}_2)] . \quad (3.5)$$

A two particle wave function of identical bosons is symmetric ("+" sign in Eq. 3.5) and in case of identical fermions - antisymmetric ("-" sign). This anti-symmetrization or symmetrization implies the correlation effect coming from the Fermi-Dirac or Bose-Einstein statistics accordingly.

To provide full description of a system consisting of two charged hadrons, one has to include in the wave function besides quantum statistics also Coulomb and strong Final State Interactions. The aim of this work is an analysis of femtoscopic radii proportional to the inverse of a width of a correlation function (for detailed description see Section 3.2.4). Since we are not interested in the direct comparison of experimental correlation functions with their analytical forms, the following simplification can be made. A width of identical particles correlation function is determined by effects coming from quantum statistics, hence one can ignore influence of Final State Interactions, which in this case is small. Taking into account only quantum statistics can reduce complexity of calculations and save computation time.

705 **3.2.3 Source emission function**

706 To describe particle emitting source, one uses a single emission function [25]:

707

$$S_A(\mathbf{x}_1, \mathbf{p}_1) = \int S(\mathbf{x}_1, \mathbf{p}_1, \mathbf{x}_2, \mathbf{p}_2, \dots, \mathbf{x}_N, \mathbf{p}_N) d\mathbf{x}_2 d\mathbf{p}_2 \dots d\mathbf{x}_N d\mathbf{p}_N \quad (3.6)$$

708 and a two-particle one:

$$S_{AB}(\mathbf{x}_1, \mathbf{p}_1, \mathbf{x}_2, \mathbf{p}_2) = \int S(\mathbf{x}_1, \mathbf{p}_1, \mathbf{x}_2, \mathbf{p}_2, \dots, \mathbf{x}_N, \mathbf{p}_N) d\mathbf{x}_3 d\mathbf{p}_3 \dots d\mathbf{x}_N d\mathbf{p}_N . \quad (3.7)$$

709 Emission function $S(\cdot)$ can be interpreted as a probability to emit a particle, or
 710 a pair of particles from a given space-time point with a given momentum. In
 711 principle, the source emission function should encode all physics aspects of the
 712 particle emission process i.e. the symmetrization for bosons and fermions, as
 713 well as the two-body and many body Final State Interactions. Instead of this,
 714 one assume that each particle's emission process is independent - the interac-
 715 tion between final-state particles after their creation is independent from their
 716 emission process. The assumption of this independence allows to construct two-
 717 particle emission function from single particle emission functions via a convolu-
 718 tion [25]:

$$S(\mathbf{k}^*, \mathbf{r}^*) = \int S_A(\mathbf{p}_1, \mathbf{x}_1) S_B(\mathbf{p}_2, \mathbf{x}_2) \delta \left[\mathbf{k}^* - \frac{\mathbf{p}_1 + \mathbf{p}_2}{2} \right] \delta [\mathbf{r}^* - (\mathbf{x}_1 + \mathbf{x}_2)] \times d^4 \mathbf{x}_1 d^4 \mathbf{x}_2 d^4 \mathbf{x}_1 d^3 \mathbf{p}_1 d^3 \mathbf{p}_2 \quad (3.8)$$

719 In case of identical particles, ($S_A = S_B$) several simplifications can be made. A
 720 convolution of the two identical Gaussian distributions is also a Gaussian distri-
 721 bution with σ multiplied by $\sqrt{2}$. Femtoscopy can give information only about
 722 two-particle emission function, but when considering Gaussian distribution as
 723 a source function in Eq. 3.8, one can obtain a σ of a single emission function
 724 from a two-particle emission function. The Eq. 3.8 is not reversible - an inform-
 725 ation about $S_A(\cdot)$ cannot be derived from $S_{AB}(\cdot)$. An exception from this rule
 726 is a Gaussian source function, hence it is often used in femtoscopic calculations.
 727 Considering pairs of identical particles, an emission function is assumed to be
 728 described by the following equation in the Pair Rest Frame [25]:

$$S_{1D}^{PRF}(\mathbf{r}^*) = \exp \left(-\frac{r_{out}^{*2} + r_{side}^{*2} + r_{long}^{*2}}{4R_{inv}^2} \right) . \quad (3.9)$$

To change from the three-dimensional variables to the one-dimensional variable
 one requires introduction of the proper Jacobian r^{*2} .

$$S_{1D}^{PRF}(r^*) = r^{*2} \exp \left(-\frac{r^{*2}}{4R_{inv}^2} \right) . \quad (3.10)$$

729 The “4” in the denominator before the “standard deviation” R_{inv} in the Gaussian
 730 distribution comes from the convolution of the two Gaussian distributions,
 731 which multiplies the R_{inv} by a factor of $\sqrt{2}$.

A more complex form of emission function was used by all RHIC and SPS experiments in identical pion femtoscopy:

$$S_{3D}^{LCMS}(\mathbf{r}) = \exp \left(-\frac{r_{out}^2}{4R_{out}^2} - \frac{r_{side}^2}{4R_{side}^2} - \frac{r_{long}^2}{4R_{long}^2} \right). \quad (3.11)$$

732 The main difference of this source function is that it has three different and inde-
 733 pendent widths R_{out} , R_{side} , R_{long} and they are defined in the LCMS, not in PRF.
 734 Unlike in PRF, in LCMS an equal-time approximation is not used. For identical
 735 particles this is not a problem - only Coulomb interaction inside a wave function
 736 depends on Δt .

737 Relationship between one-dimensional and three-dimensional source sizes

738 Up to now, most of femtoscopic measurements were limited only to averaged
 739 source size R_{av}^L (the letter “L” in superscript stands for LCMS):

$$S_{1D}^{LCMS}(\mathbf{r}) = \exp \left(-\frac{r_{out}^2 + r_{side}^2 + r_{long}^2}{2R_{av}^L} \right). \quad (3.12)$$

740 The relationship between between $S_{1D}^{LCMS}(\cdot)$ and $S_{3D}^{LCMS}(\cdot)$ is given by:

$$S_{3D}^{LCMS}(r) = \int \exp \left(-\frac{r_{out}^2}{2R_{out}^L} - \frac{r_{side}^2}{2R_{side}^L} - \frac{r_{long}^2}{2R_{long}^L} \right) \times \delta \left(r - \sqrt{r_{out}^2 + r_{side}^2 + r_{long}^2} \right) dr_{out} dr_{side} dr_{long}. \quad (3.13)$$

741 The one-dimensional source size corresponding to the three-dimensional one can
 742 be approximated by the following form:

$$S_{1D}^{LCMS}(r) = r^2 \exp \left(-\frac{r^2}{2R_{av}^L} \right). \quad (3.14)$$

743 The equation above assumes that $R_{out}^L = R_{side}^L = R_{long}^L$ hence $R_{av}^L = R_{out}^L$. If this
 744 condition is not satisfied, one can not give explicit mathematical relation between
 745 one-dimensional and three-dimensional source sizes. However, for realistic val-
 746 ues of R (i.e. for similar values of R_{out} , R_{side} , R_{long}), the S_{3D}^{LCMS} from Eq. 3.13 is
 747 not very different from Gaussian distribution and can be well approximated by
 748 Eq. 3.13.

749 A deformation of an averaged source function in case of big differences in
 750 R_{out} , R_{side} , R_{long} is presented in the Fig. 3.3. A three-dimensional Gaussian dis-
 751 tribution with varying widths was averaged into one-dimensional function using

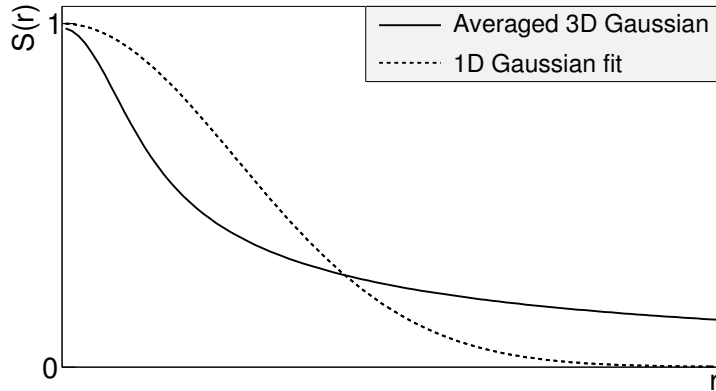


Figure 3.3: An averaged three-dimensional Gaussian source function with different widths was averaged into one-dimensional function. To illustrate deformations, one-dimensional Gaussian distribution was fitted.

the Eq. 3.13. Afterwards, an one-dimensional Gaussian distribution was fitted.
One can notice a heavy tail of an averaged distribution in long r region, which
makes an approximation using one-dimensional distribution in this case quite
inaccurate.

Using Eq. 3.13 and Eq. 3.14 one can obtain a relation between one-dimensional width and the three-dimensional ones. Through numerical calculations one can find the following approximate relation [25]:

$$R_{av}^L = \sqrt{\left(R_{out}^{L^2} + R_{side}^{L^2} + R_{long}^{L^2}\right)/3}. \quad (3.15)$$

This equation does not depend on the pair velocity, hence it is valid in the LCMS and PRF.

3.2.4 Analytical form of a correlation function

The fundamental object in a particle interferometry is a correlation function. The correlation function is defined as:

$$C(\mathbf{p}_a, \mathbf{p}_b) = \frac{P_2(\mathbf{p}_a, \mathbf{p}_b)}{P_1(\mathbf{p}_a)P_1(\mathbf{p}_b)}, \quad (3.16)$$

where P_2 is a conditional probability to observe a particle with momentum \mathbf{p}_b if particle with momentum \mathbf{p}_a was also observed. A P_1 is a probability to observe a particle with a given momentum. The relationship between source emission function, pair wave function and the correlation function is described by the following equation:

$$C(\mathbf{p}_1, \mathbf{p}_2) = \int S_{AB}(\mathbf{p}_1, \mathbf{x}_1, \mathbf{p}_2, \mathbf{x}_2) |\Psi_{AB}|^2 d^4\mathbf{x}_1 d^4\mathbf{x}_2 \quad (3.17)$$

Substituting the one-dimensional emission function (Eq. 3.10) into the integral above yields the following form of correlation function in PRF:

$$C(q) = 1 + \lambda \exp(-R_{inv}^2 q^2) \quad (3.18)$$

where q is a momentum difference between two particles. When using the three-dimensional emission function (Eq. 3.11) one gets the following correlation function defined in the LCMS:

$$C(\mathbf{q}) = 1 + \lambda \exp(-R_{out}^2 q_{out}^2 - R_{side}^2 q_{side}^2 - R_{long}^2 q_{long}^2) \quad (3.19)$$

where q_{out} , q_{side} , q_{long} are \mathbf{q} components in the outward, sideward and longitudinal direction. The λ parameter in the equations above determines correlation strength. The lambda parameter has values in the range $\lambda \in [-0.5, 1]$ and it depends on a pair type. In case of pairs of identical bosons (like $\pi\pi$ or KK) the lambda parameter $\lambda \rightarrow 1$. For identical fermions (e.g. $p-p$) $\lambda \rightarrow -0.5$. Values of λ observed experimentally are lower than 1 (for bosons) and greater than -0.5 (for fermions). There are few explanations to this effect: detector efficiencies, inclusion of misidentified particles in a used sample or inclusion of non-correlated pairs (when one or both particles come from e.g. long-lived resonance). The analysis carried out in this work uses data from a model, therefore the detector efficiency and particle purity is not taken into account [25].

3.2.5 Spherical harmonics decomposition of a correlation function

Results coming from an analysis using three-dimensional correlation function in Cartesian coordinates are quite difficult to visualize. To do that, one usually performs a projection into one dimension in outward, sideward and longitudinal directions. One may loose important information about a correlation function in this procedure, because it gives only a limited view of the full three-dimensional structure. Recently, a more advanced way of presenting correlation function - a spherical harmonics decomposition, was proposed. The three-dimensional correlation function is decomposed into an infinite set of components in a form of one-dimensional histograms $C_l^m(q)$. In this form, a correlation function is defined as a sum of a series [26]:

$$C(\mathbf{q}) = \sum_{l,m} C_l^m(q) Y_l^m(\theta, \phi), \quad (3.20)$$

where $Y_l^m(\theta, \phi)$ is a spherical harmonic function. Spherical harmonics are an orthogonal set of solutions to the Laplace's equation in spherical coordinates. Hence, in this approach, a correlation function is defined as a function of q , θ and ϕ . To obtain C_l^m coefficients in the series, one has to calculate the following integral:

$$C_l^m(q) = \int_{\Omega} C(q, \theta, \phi) Y_l^{m*}(\theta, \phi) d\Omega, \quad (3.21)$$

793 where Ω is a full solid angle.

Spherical harmonics representation has several important advantages. The main one is that it requires less statistics than traditional analysis performed in Cartesian coordinates. Another one is that it encodes full three-dimensional information in a set of one-dimensional plots. In principle it does not have to be an advantage, because full description of a correlation function requires infinite number of l, m components. But it so happens that the intrinsic symmetries of a pair distribution in a femtoscopic analysis result in most of the components to vanish. For the identical particles correlation functions, all coefficients with odd values of l and m disappear. It has also been shown, that the most significant portion of femtoscopic data is stored in the components with the lowest l values. It is expected that, the main femtoscopic information is contained in the following components [25]:

$$C_0^0 \rightarrow R_{LCMS}, \quad (3.22)$$

$$\Re C_2^0 \rightarrow \frac{R_T}{R_{long}}, \quad (3.23)$$

$$\Re C_2^2 \rightarrow \frac{R_{out}}{R_{side}}, \quad (3.24)$$

794 where $R_{LCMS} = \sqrt{(R_{out}^2 + R_{side}^2 + R_{long}^2)/3}$ and $R_T = \sqrt{(R_{out}^2 + R_{side}^2)/2}$.

795 The C_0^0 is sensitive to the overall size of a correlation function. The $\Re C_2^0$ carries
 796 the information about the ratio of the transverse to the longitudinal radii, due
 797 to its $\cos^2(\theta)$ weighting in Y_2^0 . The component $\Re C_2^2$ with its $\cos^2(\phi)$ weighting
 798 encodes the ratio between outward and sideward radii. Thus, the spherical har-
 799 monics method allows to obtain and analyze full three-dimensional femtoscopic
 800 information from a correlation function [25].

801 3.3 Experimental approach

802 The correlation function is defined as a probability to observe two particles
 803 together divided by the product of probabilities to observe each of them sepa-
 804 rately (Eq. 3.16). Experimentally this is achieved by dividing two distributions
 805 of relative momentum of pairs of particles coming from the same event and the
 806 equivalent distribution of pairs where each particle is taken from different colli-
 807 sions. In this way, one obtains not only femtoscopic information but also all other
 808 event-wide correlations. This method is useful for experimentalists to estimate
 809 the magnitude of non-femtoscopic effects. There exists also a different approach,
 810 where two particles in pairs in the second distribution are also taken from the
 811 same event. The second method gives only information about physical effects
 812 accessible via femtoscopy. The aim of this work is a study of effects coming from
 813 two particle interferometry, hence the latter method was used.

814 In order to calculate experimental correlation function, one uses the follow-
 815 ing approach. One has to construct two histograms: the *numerator* N and the

816 denominator D with the particle pairs momenta, where particles are coming from
 817 the same event. Those histograms can be one-dimensional (as a function of $|\mathbf{q}|$),
 818 three dimensional (a function of three components of \mathbf{q} in LCMS) or a set of one-
 819 dimensional histogram representing components of the spherical harmonic de-
 820 composition of the distribution. The second histogram, D is filled for each pair
 821 with the weight 1.0 at a corresponding relative momentum $\mathbf{q} = 2\mathbf{k}^*$. The first one,
 822 N is filled with the same procedure, but the weight is calculated as $|\Psi_{ab}(\mathbf{r}^*, \mathbf{k}^*)|^2$.
 823 A division N/D gives the correlation function C . This procedure can be simply
 824 written as [25]:

$$C(\mathbf{k}^*) = \frac{N}{D} = \frac{\sum_{n_i \in D} \delta(\mathbf{k}_i^* - \mathbf{k}^*) |\Psi_{ab}(\mathbf{r}_i^*, \mathbf{k}_i^*)|^2}{\sum_{n_i \in D} \delta(\mathbf{k}_i^* - \mathbf{k}^*)} . \quad (3.25)$$

The D histogram represents the set of all particle pairs used in calculations.
 The n_i is a pair with the its relative momentum \mathbf{k}_i^* and relative separation \mathbf{r}_i^* .
 Mathematically, the procedure of calculating the Eq. 3.25 is equivalent to a
 calculation of an integral in Eq. 3.17 through a Monte-Carlo method. The wave
 function used in Eq. 3.25 has one of the following forms:

$$|\Psi_{\pi\pi}(\mathbf{r}^*, \mathbf{k}^*)|^2 = |\Psi_{KK}(\mathbf{r}^*, \mathbf{k}^*)|^2 = 1 + \cos(2\mathbf{k}^* \mathbf{r}^*) , \quad (3.26)$$

$$|\Psi_{pp}(\mathbf{r}^*, \mathbf{k}^*)|^2 = 1 - \frac{1}{2} \cos(2\mathbf{k}^* \mathbf{r}^*) . \quad (3.27)$$

825 The first one is used in case of bosons, and the latter one is for identical fermions.
 826 A wave function for pair of spin-1/2 fermions (Eq. 3.27) is a superposition of two
 827 possible states: singlet state (with spin equal to 0 and one eigenstate) and triplet
 828 state (with spin equal to 1 and three possible eigenstates). For a singlet state, a
 829 wave function is symmetric, and for triplet state, it is antisymmetric. In other
 830 words the $|\Psi_{pp}|^2$ encodes correlation coming from Bose-Einstein statistics (with
 831 weight 1/4) and anti-correlation from Fermi-Dirac distribution (with weight 3/4).

832 3.4 Scaling of femtoscopy radii

833 A particle interferometry formalism presented in the previous sections as-
 834 sumes that particle emitting source is static. This is not the case in heavy ion
 835 collisions at LHC. An existence of transverse radial and elliptic flow suggest that
 836 created system is dynamic. To address this issue, a concept of *lengths of homogen-*
 837 *eity* was introduced. It is defined as:

$$\frac{|f(p, x + \lambda) - f(p, x)|}{f(p, x)} = 1 , \quad (3.28)$$

838 where λ is the homogeneity length. It can be interpreted as the distance at which
 839 relative change of the source Wigner function f becomes large. One can measure

the lengths of homogeneity of a system using femtoscopic radii. This concept can be intuitively explained on a basis of hydrodynamic models. Each source element is emitting particles with a velocity which is a combination of two components: a fluid cell velocity β_f (which is taken from the flow field $u_\mu(x^\mu)$) and thermal velocity β_{th} (which has random direction). These particles can combine into pairs of small relative momenta and become correlated. If two particles are emitted far ($|x_a - x_b| > \lambda$) away from each other, the flow field u_μ in their point of emission might be very different and it will be impossible for them to have sufficiently small relative momenta to be in the region of interference effect. This effect is presented in Fig. 3.4. An increase of a correlation is visible for pairs with low relative momenta [8].

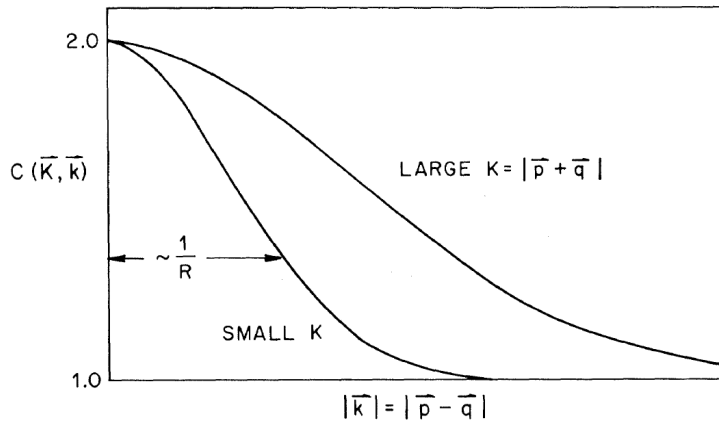


Figure 3.4: Correlation function width dependence on total pair momentum. Pion pairs with a large total momentum have a wider correlation (smaller apparent source) [27].

850

851 3.4.1 Scaling in LCMS

Hydrodynamic calculations performed in LCMS show that femtoscopic radii in outward, sideward, and longitudinal direction show dependence on transverse mass $m_T = \sqrt{k_T^2 + m^2}$, where m is a mass of a particle [28]. Moreover, experimental results show that this scaling is observed for R_{LCMS} radii also. This dependence can be expressed as follows:

$$R_i = \alpha m_T^{-\beta} \quad (3.29)$$

852 where i subscript indicates that this equation applies to R_{out} , R_{side} and R_{long}
 853 radii. The β exponent is approximately equal 0.5. In case of strong transversal
 854 expansion of the emitting source, the decrease of longitudinal interferometry ra-
 855 dius can be more quick than $m_T^{-0.5}$, hence one can expect for longitudinal radii
 856 greater values of $\beta > 0.5$ [28].

3.4.2 Scaling in PRF

In the collisions at the LHC energies, pions are most abundant particles and their multiplicities are large enough to enable three-dimensional analysis. However, for heavier particles, such as kaons and protons statistical limitations arise. Hence it is often possible to only measure one-dimensional direction-averaged radius R_{inv} for those particles. The R_{inv} is then calculated in the PRF. The transition from LCMS to PRF is a Lorentz boost in the direction of pair transverse momentum with velocity $\beta_T = p_T/m_T$. Hence only R_{out} changes:

$$R_{out}^* = \gamma_T R_{out}. \quad (3.30)$$

A Lorentz factor $\gamma_T = m_T/m$ depends on the particle type, therefore for the lighter particles (and for the same m_T) γ_T is much larger, which causes bigger growth of R_{out} and overall radius. This transformation to PRF breaks the scaling observed in the LCMS radii.

This increase of radius in the outward direction induces overall source size growth and whatsoever the source distribution function becomes non-gaussian. In this case the source function is developing long-range tails and its one-dimensional projection is much narrower than Gaussian distribution. This deformation is presented in Fig. 3.3. The influence of these effects can be expressed with an approximate formula:

$$R_{inv} = \sqrt{(R_{out}^2 \sqrt{\gamma_T} + R_{side}^2 + R_{long}^2)/3}. \quad (3.31)$$

Because the averaging of the radii is done in quadrature, one would have expected appearance of γ_T^2 instead of $\sqrt{\gamma_T}$ in this equation. However the Monte-Carlo procedure shows that this is not the case and the actual growth is smaller than the naive expectation. Numerical simulations yield that this increase is best described with the $\sqrt{\gamma_T}$ in the Eq. 3.31 [29].

Assuming that radii in all directions are equal $R_{out} = R_{side} = R_{long}$, Eq. 3.31 can be reverted using Eq. 3.15 to express relationship between LCMS and PRF overall radii [29]:

$$R_{LCMS} \approx R_{inv} \times [(\sqrt{\gamma_T} + 2)/3]^{-1/2}. \quad (3.32)$$

This approximate formula allows to restore power-law behaviour of the scaled radii not only when the radii are equal, but also when their differences are small (for explanation see the last part of the Section 3.2.3).

This method of recovering scaling in PRF can be used as a tool for the search of hydrodynamic collectivity between pions, kaons and protons in heavy ion collisions with the measurement of one-dimensional radius in PRF.

886 **Chapter 4**

887 **Results**

888 For the purposes of the femtoscopic analysis in this thesis, the THERMINATOR
889 model was used to generate large number of events for eight different sets of
890 initial conditions corresponding the following centrality ranges: 0-5%, 0-10%, 10-
891 20%, 20-30%, 30-40%, 40-50%, 50-60% and 60-70% for the Pb-Pb collisions at the
892 centre of mass energy $\sqrt{s_{NN}} = 2.76 \text{ TeV}$.

893 **4.1 Identical particles correlations**

894 The correlation functions (three-dimensional and one-dimensional) were cal-
895 culated separately for the following different pairs of identical particles: π - π , K -
896 K and p - p for nine k_T bins (in GeV/c): 0.1-0.2, 0.2-0.3, 0.3-0.4, 0.4-0.5, 0.6-0.7,
897 0.7-0.8, 0.8-1.0 and 1.0-1.2. In case of kaons, k_T ranges start from 0.3 and for pi-
898 ons from 0.4 and for both of them the maximum value is 1.0. The k_T ranges for
899 the heavier particles were limited to maintain sufficient multiplicity to perform
900 reliable calculations.

901 **4.1.1 Spherical harmonics components**

902 The three-dimensional correlation function as a function of relative
903 momentum q_{LCMS} was calculated in a form of components of spherical
904 harmonics series accordingly to the Eq. 3.21. In the femtoscopic analysis of
905 identical particles, the most important information is stored in the $\Re C_0^0$, $\Re C_2^0$
906 and $\Re C_2^2$, hence only those components were analyzed. Correlation functions
907 obtained in this procedure were calculated for the different centrality bins for the
908 pairs of pions, kaons and protons. They are presented in the Fig. 4.1, 4.2 and 4.3.

909 Coefficients for pairs of identical bosons (pions and kaons) are shown in the
910 Fig. 4.1 and 4.2. The wave function symmetrization (Bose-Einstein statistics)
911 causes the increase of a correlation in the low relative momenta regime ($q_{LCMS} <$
912 0.06 GeV/c or even $q_{LCMS} < 0.12$ GeV/c for more peripheral collisions). It is
913 clearly visible in the $\Re C_0^0$ component. The $\Re C_0^0$ resembles one-dimensional cor-

relation function and in fact it encodes information about overall source radius. The second coefficient $\Re C_2^0$ differs from zero (is negative), which yields the information about the ratio R_T/R_{long} . The $\Re C_2^2$ stores the R_{out}/R_{side} ratio and one can notice that is non-vanishing (is also negative).

The correlation function for a pair of identical fermions is presented in the Fig. 4.3. An influence of wave function anti-symmetrization (Fermi-Dirac statistics) has its effect in the decrease of a correlation down to 0.5 at low relative momentum ($q_{LCMS} < 0.1 \text{ GeV/c}$ or $q_{LCMS} < 0.15 \text{ GeV/c}$ for more peripheral collisions), which can be observed in $\Re C_0^0$. The $\Re C_2^0$ and $\Re C_2^2$ coefficients differ from zero and are becoming positive.

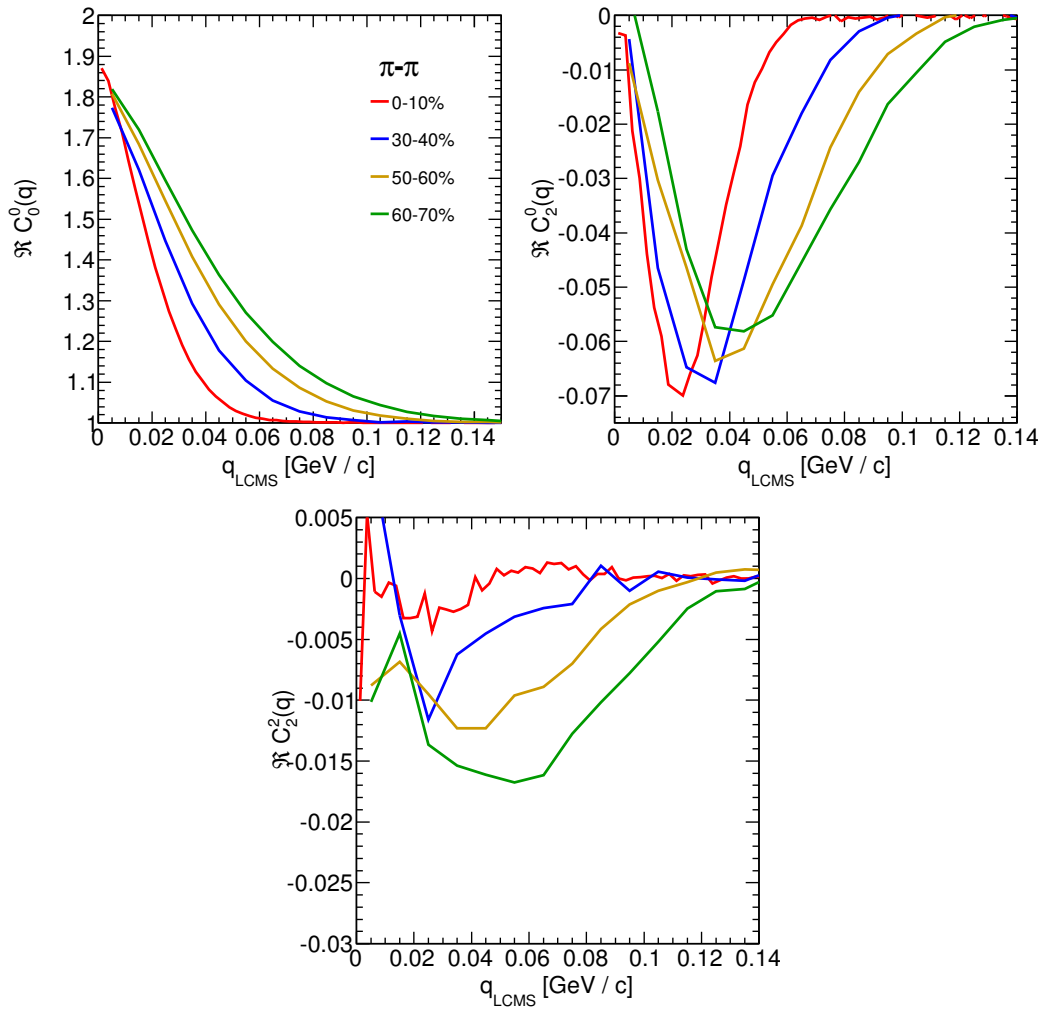


Figure 4.1: Spherical harmonics coefficients of the two-pion correlation function. From the top left: $\Re C_0^0$, $\Re C_2^0$ and $\Re C_2^2$. Only few centrality bins are presented for increased readability.

924 The common effect of the spherical harmonics form of a correlation function
 925 is the “mirroring” of the shape of the $\Re C_0^0$ coefficient - when correlation func-
 926 tion increases at low q_{LCMS} , the $\Re C_2^0$ and $\Re C_2^2$ are becoming negative and vice
 927 versa. This is quite different behaviour than in the case of correlations of non-
 928 identical particles, where the $\Re C_2^0$ still behaves in the same manner, but $\Re C_2^2$ has
 929 the opposite sign to the $\Re C_2^0$ [25].

930 In all cases, the correlation function gets wider with the peripherality of a
 931 collision i.e. the correlation function for most central collisions (0-10%) is much
 932 narrower than for the most peripheral ones (60-70%). This phenomena in clearly

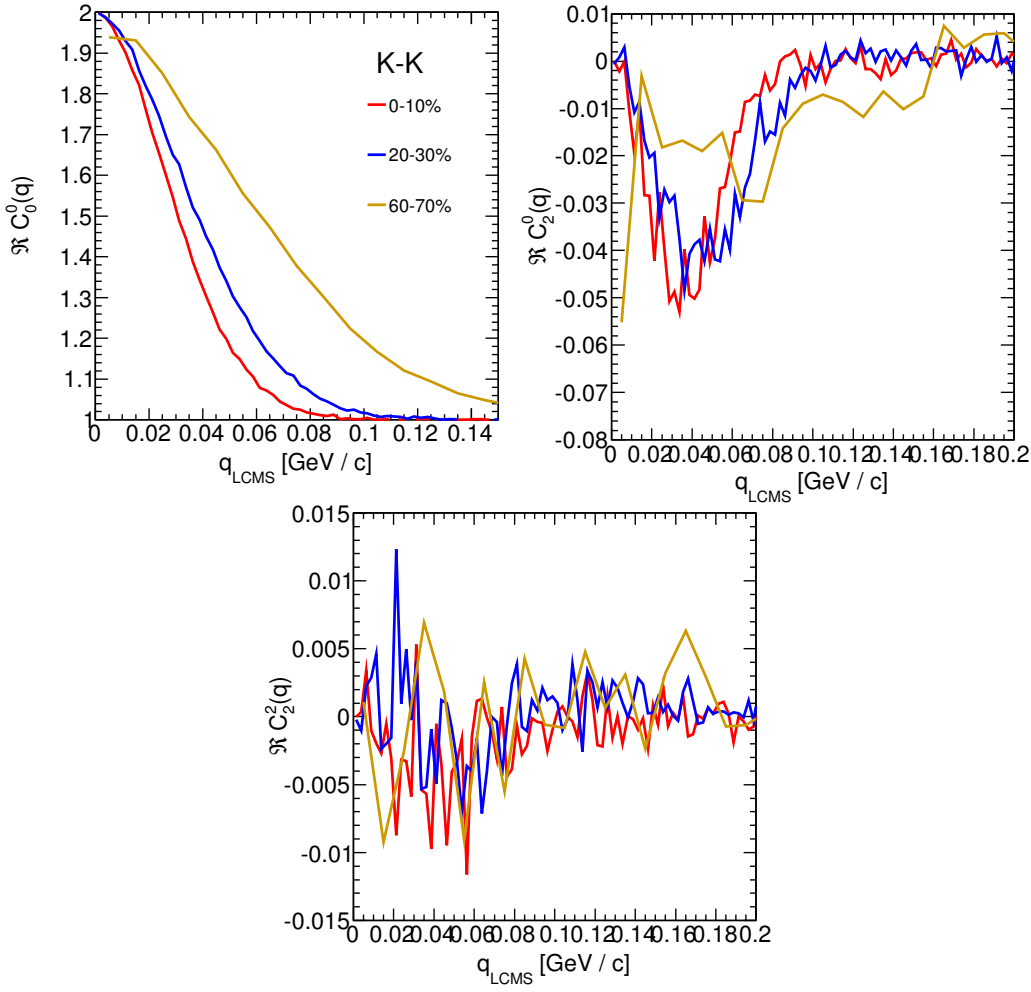


Figure 4.2: Spherical harmonics coefficients of the two-kaon correlation function. From the top left: $\Re C_0^0$, $\Re C_2^0$ and $\Re C_2^2$. Only few centrality bins are presented for increased readability. The $\Re C_2^2$ is noisy, but one can still notice that it differs from zero and is becoming negative.

visible the $\Re C_0^0$ coefficients. Other components are also affected by this effect, this is especially noticeable in the case of kaons and pions. For the protons, the results are noisy, hence this effect is not clearly distinguishable.

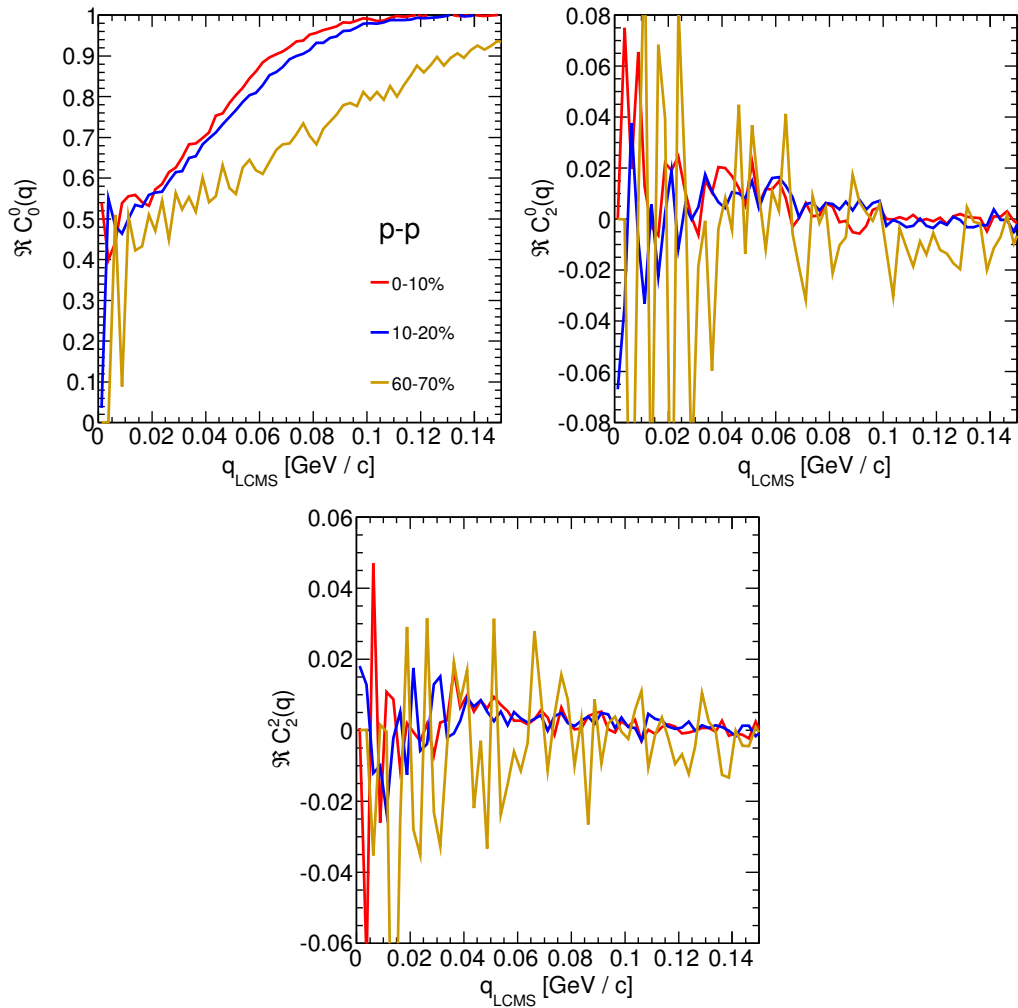
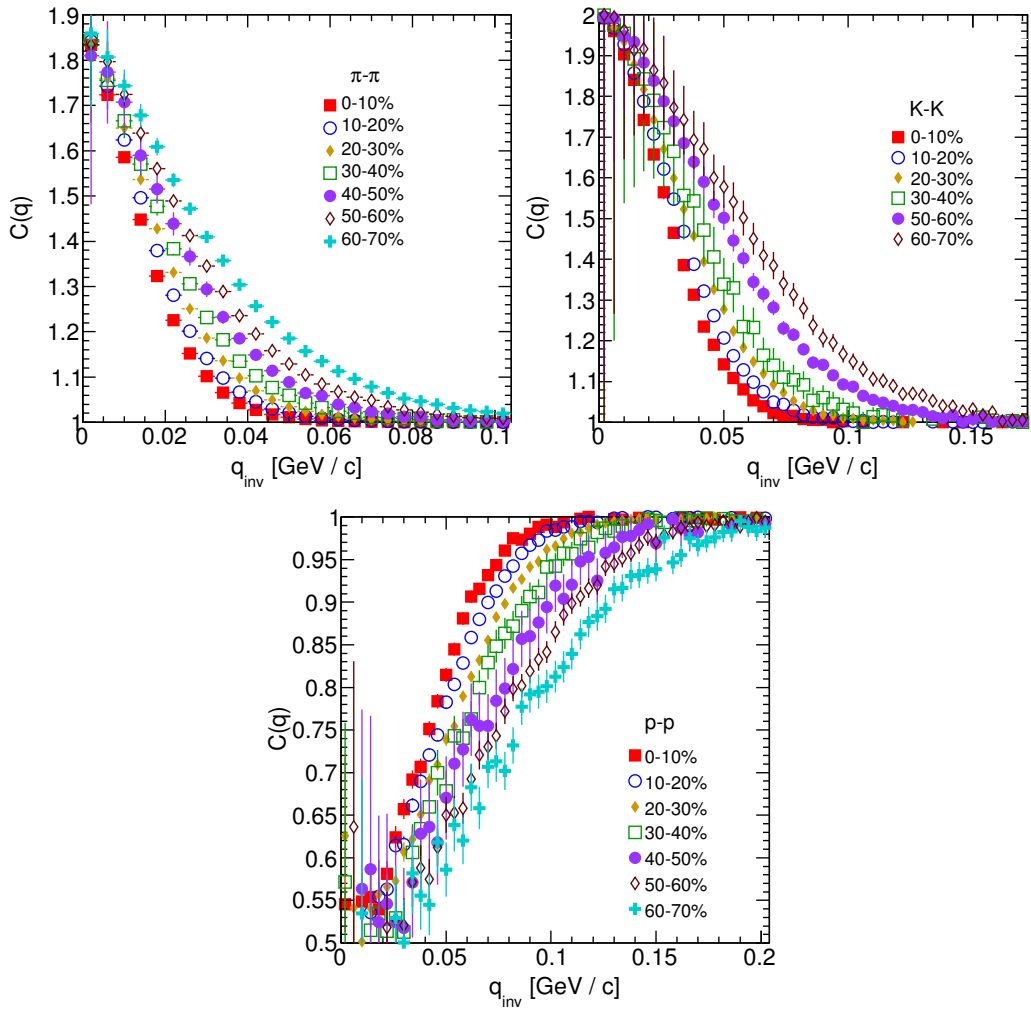


Figure 4.3: Spherical harmonics coefficients of the two-proton correlation function. From the top left: $\Re C_0^0$, $\Re C_2^0$ and $\Re C_2^2$. Only few centrality bins are presented for increased readability. The $\Re C_2^0$ and $\Re C_2^2$ are noisy, but one can still notice, that they differ from zero and are becoming positive.

936 **4.1.2 Centrality dependence of a correlation function**

937 The centrality dependence of a correlation function is especially visible in
938 one-dimensional correlation functions. This effect is presented in the Fig. 4.4 -
939 the correlation functions for pions, kaons and protons are plotted for the same
940 k_T range but different centrality bins. One can notice that the width of a func-
941 tion is smaller in the case of most central collisions. Hence, the femtoscopic radii
942 (proportional to the inverse of width) are increasing with the centrality. An ex-
943 planation for this growth is that in the most central collisions, a size of a created
system is larger than for the peripheral ones.



944 Figure 4.4: One-dimensional correlation function for pions (top left), kaons (top right) and protons (bottom) for different centralities.

945 **4.1.3 k_T dependence of a correlation function**

946 In the Fig. 4.5 there are presented one-dimensional correlation functions for
 947 pions, kaons and protons for the same centrality bin, but different k_T ranges. One
 948 can observe in all cases of the particle types, appearance of the same trend: with
 949 the increase of the total transverse momentum of a pair, the width of a correlation
 950 function increases and the femtoscopic radius decreases. The plots in the Fig. 4.5
 951 were zoomed in to show the influence of k_T .

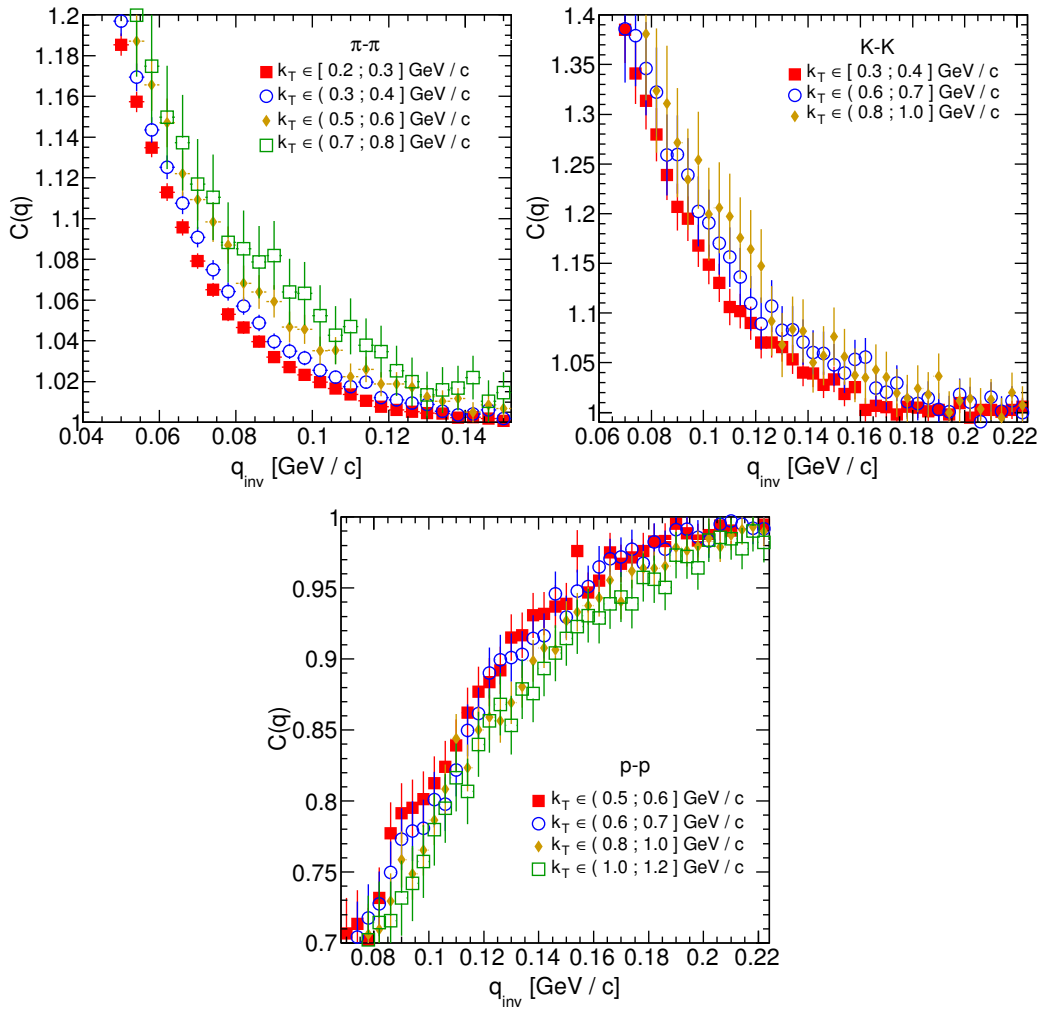


Figure 4.5: One-dimensional correlation functions for pions, kaons and protons, for the same centrality bin and different k_T ranges. The plot was zoomed in to the region which illustrates the k_T dependence in the best way. Only few of the calculated ranges are presented for better readability.

4.2 Results of the fitting procedure

In order to perform a quantitative analysis of a wide range of correlation functions, the theoretical formulas were fitted to the calculated experimental-like data. In this procedure, the femtoscopic radii for the three-dimensional as well as one-dimensional correlation functions were extracted. The main goal of this analysis is a verification of a common transverse mass scaling for different particles types. Obtained radii are plotted as a function of a transverse mass $m_T = \sqrt{k_T^2 + m^2}$. To test the scaling, the following power-law was fitted to the particular radii afterwards:

$$R_x = \alpha m_T^{-\beta}, \quad (4.1)$$

where the α and β are free parameters.

4.2.1 The three-dimensional femtoscopic radii scaling

In the Fig. 4.6 there are presented femtoscopic radii in the outward, sideward and longitudinal directions for the analysis of two-pion correlation functions in

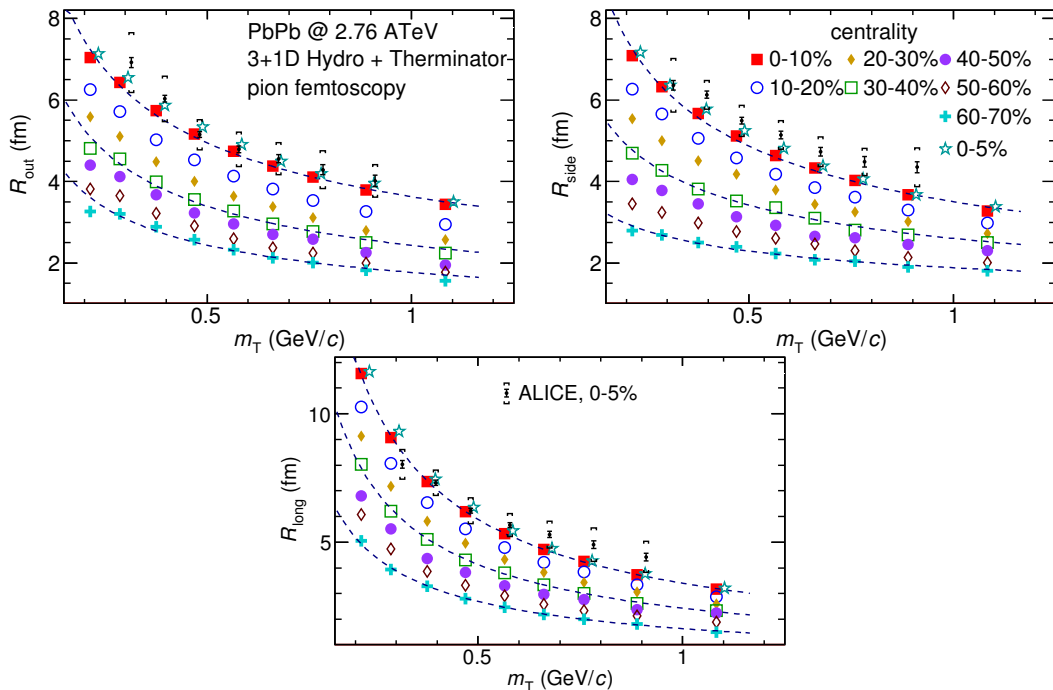


Figure 4.6: Femtoscopic radii in LCMS coming from two-pion correlation functions for all centrality bins as a function of m_T . The dashed lines are power-law fits. The most central collisions (0-5%) are compared to the results from ALICE [30]. The two datasets are shifted to the right for visibility [29].

the LCMS. The dashed lines are fits of the power law to the data. One can notice, that the power law describes well data points with a 5% accuracy. The β fit parameter for the outward direction is in the order of 0.45. For the sideward direction, this parameter has the similar value, but it is lower for the most peripheral collisions. In case of the longitudinal direction, the β has greater value, up to 0.75. In the Fig. 4.6 there are also compared results for the top 5% central collisions (star-shaped markers) with experimental data from ALICE [30]. The experimental results are consistent with the ones coming from the model predictions.

The Fig. 4.7 presents femtoscopic radii coming from the kaon calculations. The R_{out} , R_{side} and R_{long} fall also with the power-law within the 5% accuracy. The β parameter was larger in case of kaons: 0.59 in outward direction, 0.54 in the sideward and 0.86 for longitudinal.

The results for two-proton analysis are shown in the Fig. 4.8. The Eq. 4.1 was fitted to the data and tells that the protons also follow the m_T scaling within 5% range. The β parameter values were even bigger for the outward (0.58), sideward (0.61) and longitudinal (1.09) directions than for the other particle types.

The Fig. 4.9 presents results for the pions, kaons and protons together as a function of m_T . Considering differences in the β value for the fits for differ-

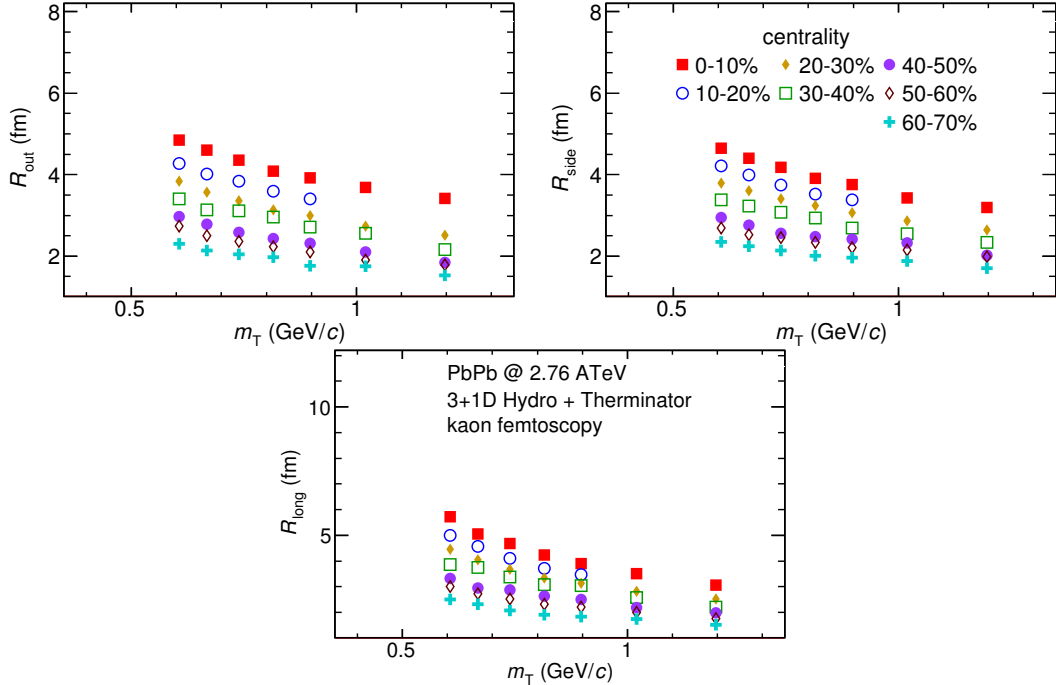


Figure 4.7: Femtoscopic radii extracted from two-kaon correlation functions for different centrality bins as a function of m_T . [29].

985 ent particles, one can suspect that there is no common scaling between different
 986 kinds of particles. However, when all of the results shown on the same plot, they
 987 are aligning on the common curve and the scaling is well preserved. The scaling
 988 accuracy is 3%, 5% and 4% for the 0-10%, 20-30% and 60-70% for the outward
 989 direction. For the sideward radii the scaling is better, with average deviations
 990 2%, 2% and 3% respectively. In case of longitudinal direction the accuracy is 6%,
 991 5% and 3% for the three centralities. The β parameter for the outward direction
 992 is close to the 0.42 in all cases. For the sideward direction it varies from 0.28 to
 993 0.47 and is bigger for more central collisions. Regarding longitudinal radii, the
 994 exponent is bigger than the other two: $\beta \in [0.62; 0.72]$. Considering all results,
 995 the plotted radii are following the common power-law scaling within the 5% ac-
 996 curacy for all directions, centralities and particle types.

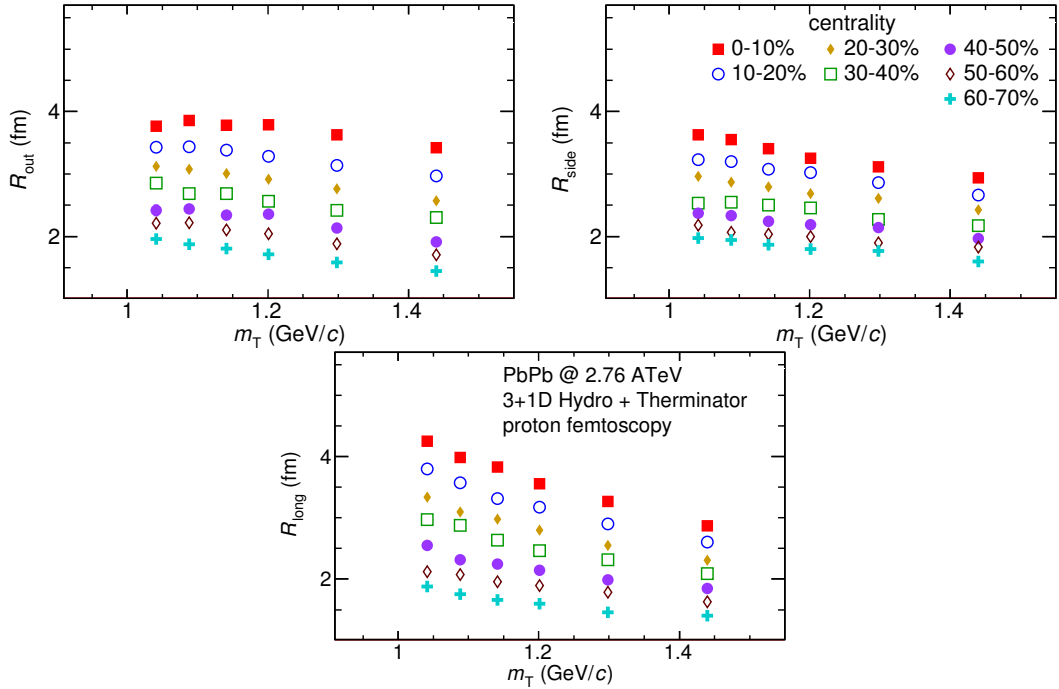


Figure 4.8: Femtoscopic radii extracted from two-proton correlation functions for different centrality bins as a function of m_T . [29].

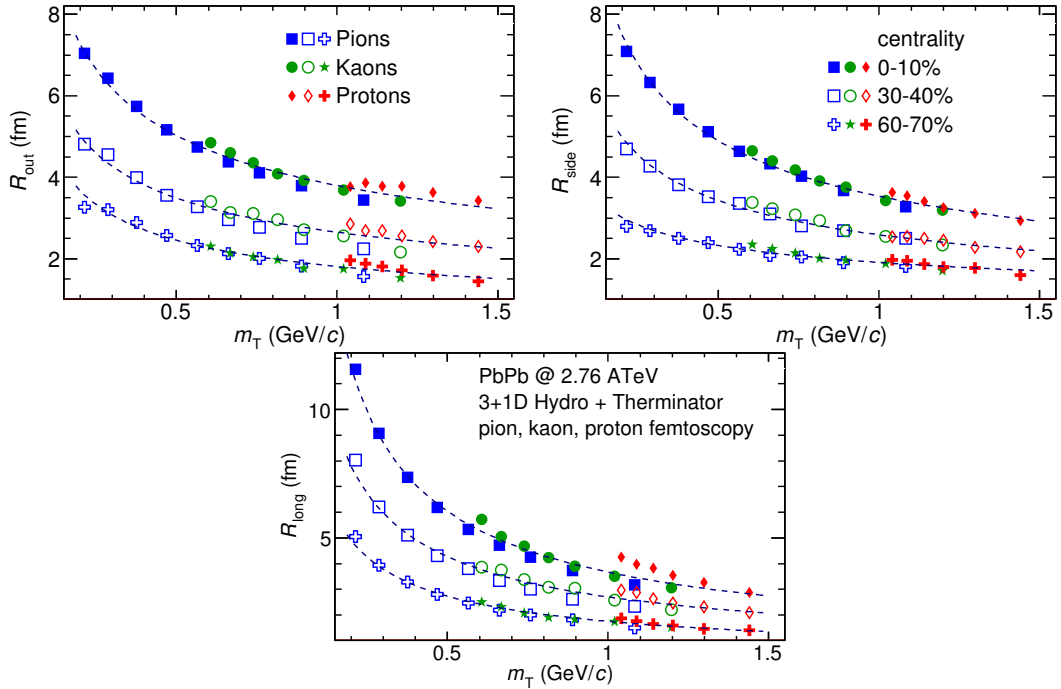


Figure 4.9: The results from the calculations for the pions, kaons and protons in for the three centralities presented on the common plot. One can notice that radii for particular centralities and different particle types follow the common power-law scaling. [29].

4.2.2 Scaling of one-dimensional radii

To the one-dimensional correlation function, the corresponding function in the PRF given by the Eq. 3.18 was fitted. The results from those fits are presented in the upper left plot in the Fig. 4.10. One immediately notices, that there is no common scaling of R_{inv} for different kind of particles. In the Fig. 4.9 the radii in the outward direction for the pions, kaons and protons for the same m_T are similar. However, when one performs a transition from the LCMS to the PRF, the R_{out} radius grows:

$$R_{out}^* = \gamma_T R_{out}, \quad (4.2)$$

where $\gamma_T = m_T/m$. For the lighter particles, the γ_T is much larger, hence the bigger growth of the R_{out} and the overall radius. This is visible in the Fig. 4.10 (top left), where the radii in the PRF for the lighter particles are bigger than for the heavier ones in case of the same m_T range.

In the Fig. 4.9 there is visible scaling in the outward, sideward and longitudinal direction. Hence one can expect an appearance of such scaling in a direction-averaged radius calculated in the LCMS. This radius is presented in the Fig. 4.10 (bottom) and indeed the R_{LCMS} exhibits power-law scaling with the m_T .

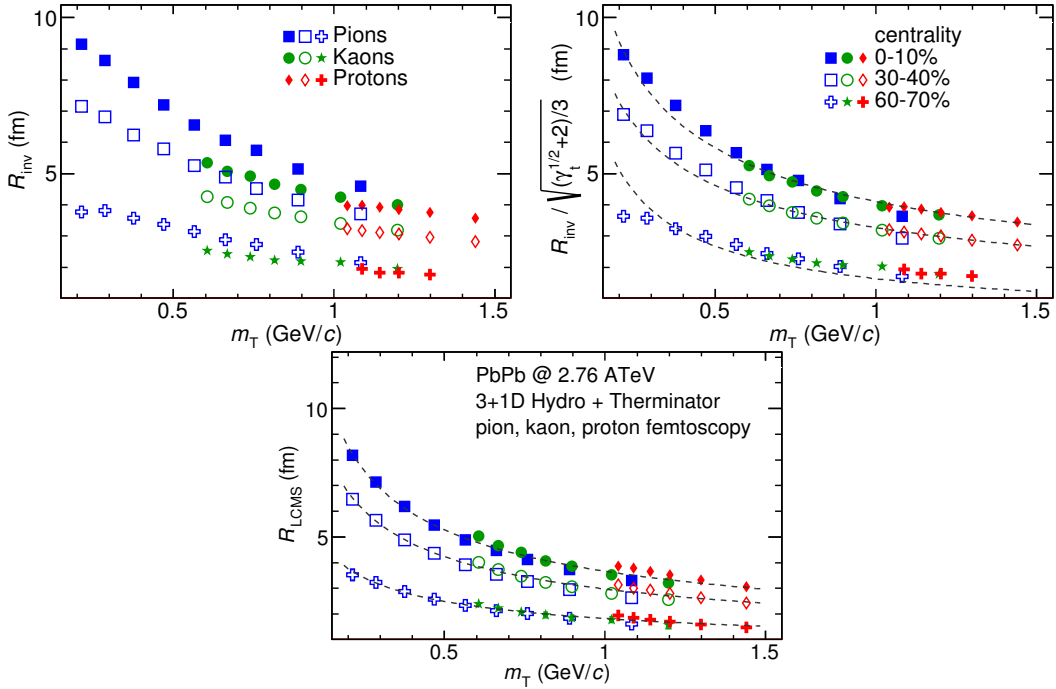


Figure 4.10: Top left: one-dimensional radius for pions, kaons and protons calculated in the PRF. Top right: the R_{inv} scaled by the proposed factor. Bottom: averaged one-dimensional radius in the LCMS for pions, kaons and protons. Only three centrality bins are shown for the better readability [29].

1013 One can try to account the effect of an increase of the radii in the outward
 1014 direction by using the appropriate scaling factor. In the Fig. 4.10 (top right) there
 1015 are femtoscopic radii in the LCMS divided by the proposed scaling factor:

$$f = \sqrt{(\sqrt{\gamma_T} + 2)/3} . \quad (4.3)$$

1016 The radii for pions, kaons and protons in the PRF after the division by f are
 1017 following the power-law with the accuracy of 10%.

1018 4.3 Discussion of the results

1019 The femtoscopic radii obtained from the three-dimensional correlation func-
 1020 tion fitting exhibit the m_T dependence described by the power law (Eq. 4.1). This
 1021 scaling is preserved quite well with accuracy <10%. Observation of such scaling
 1022 in a femtoscopic radii is a strong signal of appearance of a collective behaviour of
 1023 a particle-emitting source created in the collision. The data used in the analysis
 1024 was coming from the hydrodynamic model, hence one can indeed expect the
 1025 appearance of this scaling. However, the results for pion femtoscopy from the
 1026 ALICE at LHC are consistent with the data from analysis performed in this thesis
 1027 (Fig. 4.6). This is a confirmation of an applicability of hydrodynamic models in a
 1028 description of an evolution of a quark-gluon plasma.

1029 The β parameter calculated in the fitting of the power-law to the femtoscopic
 1030 radii is in the order of 0.5 in case of the radii in the transverse plane. This value is
 1031 consistent with the hydrodynamic predictions. In case of longitudinal radii, the
 1032 exponent is bigger (greater than 0.7), which is an indication of a strong transversal
 1033 expansion in the system [28].

1034 A scaling described above is visible in the LCMS, however due to limited stat-
 1035 istics, analysis in this reference frame is not always possible. In such case one per-
 1036 forms calculations in the PRF. The m_T scaling in the PRF is not observed - this has
 1037 the trivial kinematic origin. A transition from the PRF to LCMS causes growth
 1038 of the radius in the outward direction and the common power-law scaling for
 1039 different particles breaks due to differences in the $\gamma_T(m_T)$ for different particle
 1040 types. However one can try to deal with the radius growth and restore the scal-
 1041 ing by multiplying the radii R_{inv} by an approximate factor $\sqrt{(\sqrt{\gamma_T} + 2)/3}$. The
 1042 scaled R_{inv} are following the power-law and could be used as a verification of
 1043 hydrodynamic behaviour in the investigated particle source.

1044 The hadronic evolution and freeze-out in the THERMINATOR is followed
 1045 by the resonance propagation and decay phase. A good accuracy of a scaling
 1046 with the power-law indicated that the inclusion of the resonances does not
 1047 break the m_T scaling. However, recent calculations including also hadron
 1048 rescattering phase indicate that the scaling between pions and kaons is broken
 1049 at the LHC [31].

1050 Conclusions

1051 This thesis presents the results of the two-particle femtoscopy of different
1052 particle kinds produced in Pb-Pb collisions at the centre of mass energy
1053 $\sqrt{s_{NN}} = 2.76$ TeV. The analysed data was generated by the THERMINATOR
1054 model using the (3+1)-dimensional hydrodynamic model.

1055 The momentum correlations were studied for three different types of particle
1056 pairs: pions, kaons and protons. The data was analyzed for eight different sets
1057 of initial conditions corresponding the following centrality ranges: 0-5%, 0-10%,
1058 10-20%, 20-30%, 30-40%, 40-50%, 50-60% and 60-70%. The correlation functions
1059 were calculated for the nine k_T bins from 0.1 GeV/c to 1.2 GeV/c. The cal-
1060 culations were performed using spherical harmonics decomposition of a three-
1061 dimensional correlation function. Using this approach, one can obtain full three-
1062 dimensional information about the source size using only the three coefficients:
1063 $\Re C_0^0$, $\Re C_2^0$ and $\Re C_2^2$. To perform further quantitative analysis, the femtoscopic
1064 radii were extracted through fitting.

1065 The calculated correlation functions show expected increase of a correlation
1066 at low relative momenta in case of identical bosons (pions and kaons) and the
1067 decrease for the identical fermions (protons) respectively. This effect is especially
1068 visible in the first spherical harmonic coefficient $\Re C_0^0$. The other two components
1069 $\Re C_2^0$ and $\Re C_2^2$ are non-vanishing and are providing information about the ratios
1070 of radii in the outward, sideward and longitudinal directions.

1071 An increase of width of a correlation function with the peripherality of a colli-
1072 sion and the k_T is observed for pions, kaons and protons. This increase of femto-
1073 scopic radii (proportional to the inverse of width) with the k_T is related with the
1074 m_T scaling predicted by the hydrodynamic calculations.

1075 Hydrodynamic equations are predicting appearance of femtoscopic radii
1076 common scaling for different kinds of particles with the $m_T^{-0.5}$ in the LCMS.
1077 In the results in this work, a common scaling for different particle types is
1078 observed in the LCMS in the outward, sideward and longitudinal direction. The
1079 direction-averaged radius R_{LCMS} also shows this power-law behaviour. The
1080 fitting of a power law $\alpha m_T^{-\beta}$ to the femtoscopic radii yielded the information,
1081 that the β exponent for the outward and sideward direction is in order of 0.5,
1082 which is consistent with the hydrodynamic predictions. For the longitudinal
1083 direction, the β is bigger (>0.7) than in the other directions which is an indication
1084 of a strong transverse flow. Femtoscopic radii in LCMS are following the

1085 power-law scaling with the accuracy <5% for pions and kaons, and <10% in case
1086 of protons.

1087 In case of the one-dimensional radii R_{inv} calculated in the PRF, no common
1088 scaling is observed. This is a consequence of a transition from the LCMS to the
1089 PRF, which causes the growth of radius in the outward direction and breaks the
1090 scaling for different particles. However, one can try to correct the influence of
1091 the R_{out} growth with an approximate factor $\sqrt{(\sqrt{\gamma_T} + 2)/3}$. After the division
1092 of the R_{inv} by the proposed factor, the scaling is restored with an accuracy <10%.
1093 In this way, the experimentally simpler measure of the one-dimensional radii can
1094 be used as a probe for the hydrodynamic collectivity.

1095 The THERMINATOR model includes hydrodynamic expansion, statistical had-
1096 ronization, resonance propagation and decay afterwards. The m_T scaling is pre-
1097 dicted from the pure hydrodynamic calculations. However, this study shows,
1098 that influence of the resonances on this scaling is less than 10%.

1099 **Appendix A**

1100 **Scripts for events generation**

1101 In order to perform analysis with sufficient statistics, a large amount of gen-
1102 erated events was required. To handle this task of generation large amount of
1103 data, a computer cluster at Faculty of Physics at Warsaw University of Techno-
1104 logy was used. This cluster consists of 20 nodes with the following hardware
1105 configuration: Intel® Core™ 2 Quad CPU Q6600 @ 2.40GHz, 8GB RAM with Sci-
1106 entific Linux 5.8. The communication between nodes is realized by the TORQUE
1107 Resource Manager [32]. To control process of launching multiple event generat-
1108 ors and collecting the data, the following scripts were written using Bash script-
1109 ing language:

1110 **skynet.sh** This is a script in a form of a batch job for TORQUE. It simply
1111 launches multiple THERMINATOR processes in the same working directory
1112 with the separate output directory for each job. This solution has two
1113 advantages: saves space and computation time. A single freeze-out
1114 hypersurface file has size about 230 MB and when running 20 instances
1115 of generator this approach allows to avoid time- and space-consuming
1116 copying of the whole THERMINATOR directory before running the
1117 application. The second advantage is a sharing of files containing
1118 information about particles' multiplicities and maximum integrands
1119 between generator processes (more detailed description is in Section 2.3).
1120 One can simply execute this batch job using the following command (an
1121 example usage):

1122 qsub -q long -t 0-19 skynet.sh -v dir=th_5.7,events=6000
1123 It adds 20 event generators (with task ids from 0 to 19) to the queue, sets
1124 the THERMINATOR directory as th_5.7 and sets a number of simulated
1125 events to 6000 for each process. One has to execute this command in the
1126 directory one level higher than th_5.7 directory.

1127 **merge_events.sh** After the generation process, one has to merge calculated
1128 events into one directory. This task requires renaming of a large number of
1129 THERMINATOR event files. Each event generator job produces files named

1130 with a certain pattern, starting from event000.root with increasing number.
1131 In order to move the event files and preserve continuity in the numbering,
1132 a simple script was written. An example of usage:
1133 find /data/source -iname "event*.root" -type f \
1134 | merge_events.sh
1135 This command will find all the event files in the directory /data/source,
1136 move and rename those files accordingly to the enumeration of events in
1137 the current working directory.

1138 Sources of these two scripts are available on-line at <https://github.com/carbolymer/msc/tree/master/alix>.

₁₁₄₀ **Appendix B**

₁₁₄₁ **Macros for fitting**

₁₁₄₂ Appendix C

₁₁₄₃ Plotting scripts

¹¹⁴⁴ Bibliography

- ¹¹⁴⁵ [1] Standard Model of Elementary Paticles - Wikipedia, the free encyclopedia
¹¹⁴⁶ http://en.wikipedia.org/wiki/standard_model.
- ¹¹⁴⁷ [2] R. Aaij et al. (LHCb Collaboration). Observation of the resonant character of
¹¹⁴⁸ the $z(4430)^-$ state. *Phys. Rev. Lett.*, 112:222002, Jun 2014.
- ¹¹⁴⁹ [3] Donald H. Perkins. *Introduction to High Energy Physics*. Cambridge University Press,
¹¹⁵⁰ fourth edition, 2000. Cambridge Books Online.
- ¹¹⁵¹ [4] G. Odyniec. *Phase Diagram of Quantum Chromo-Dynamics* - course at Faculty
¹¹⁵² of Physics, Warsaw University of Technology, Jun 2012.
- ¹¹⁵³ [5] J. Beringer et al. (Particle Data Group). The Review of Particle Physics. *Phys.*
¹¹⁵⁴ *Rev.*, D86:010001, 2012.
- ¹¹⁵⁵ [6] Z. Fodor and S.D. Katz. The Phase diagram of quantum chromodynamics.
¹¹⁵⁶ 2009.
- ¹¹⁵⁷ [7] F. Karsch. Lattice results on QCD thermodynamics. *Nuclear Physics A*, 698(1-
¹¹⁵⁸ 4):199 – 208, 2002.
- ¹¹⁵⁹ [8] Adam Kisiel. *Studies of non-identical meson-meson correlations at low relative ve-*
¹¹⁶⁰ *locities in relativistic heavy-ion collisions registered in the STAR experiment*. PhD
¹¹⁶¹ thesis, Warsaw University of Technology, Aug 2004.
- ¹¹⁶² [9] J. Bartke. *Relativistic Heavy Ion Physics*. World Scientific Pub., 2009.
- ¹¹⁶³ [10] W. Florkowski. *Phenomenology of Ultra-Relativistic Heavy-Ion Collisions*.
¹¹⁶⁴ World Scientific, 2010.
- ¹¹⁶⁵ [11] Science Grid This Week, October 25, 2006 - Prob-
¹¹⁶⁶ ing the Perfect Liquid with the STAR Grid
¹¹⁶⁷ http://www.interactions.org/sgtw/2006/1025/star_grid_more.html.
- ¹¹⁶⁸ [12] K. Grebieszkow. Fizyka zderzeń ciężkich jonów,
¹¹⁶⁹ <http://www.if.pw.edu.pl/~kperl/hip/hip.html>.
- ¹¹⁷⁰ [13] Ulrich W. Heinz. From SPS to RHIC: Maurice and the CERN heavy-ion
¹¹⁷¹ programme. *Phys.Scripta*, 78:028005, 2008.

- 1172 [14] J. Adams et al. Identified particle distributions in pp and Au+Au collisions
1173 at $s(\text{NN})^{**}(1/2) = 200 \text{ GeV}$. *Phys.Rev.Lett.*, 92:112301, 2004.
- 1174 [15] G. David, R. Rapp, and Z. Xu. Electromagnetic Probes at RHIC-II. *Phys.Rept.*,
1175 462:176–217, 2008.
- 1176 [16] A. Marin et al. Dilepton measurements with CERES. *PoS*, CPOD07:034,
1177 2007.
- 1178 [17] J. Adams et al. Experimental and theoretical challenges in the search for the
1179 quark gluon plasma: The STAR Collaboration’s critical assessment of the
1180 evidence from RHIC collisions. *Nucl.Phys.*, A757:102–183, 2005.
- 1181 [18] Adam Kisiel, Tomasz Taluc, Wojciech Broniowski, and Wojciech
1182 Florkowski. THERMINATOR: THERMal heavy-IoN generATOR. *Comput.Phys.Commun.*, 174:669–687, 2006.
- 1184 [19] Mikolaj Chojnacki, Adam Kisiel, Wojciech Florkowski, and Wojciech Bro-
1185 niowski. THERMINATOR 2: THERMal heavy IoN generATOR 2. *Comput.Phys.Commun.*, 183:746–773, 2012.
- 1187 [20] I. et al (BRAHMS Collaboration) Bearden. Charged meson rapidity distri-
1188 butions in central Au + Au collisions at $\sqrt{s_{\text{NN}}} = 200 \text{ GeV}$. *Phys. Rev. Lett.*,
1189 94:162301, Apr 2005.
- 1190 [21] W. Israel and J.M. Stewart. Transient relativistic thermodynamics and kin-
1191 etic theory. *Annals of Physics*, 118(2):341 – 372, 1979.
- 1192 [22] Piotr Bożek. Flow and interferometry in (3 + 1)-dimensional viscous hydro-
1193 dynamics. *Phys. Rev. C*, 85:034901, Mar 2012.
- 1194 [23] K. Kovtun, P. D. T. Son, and A. O. Starinets. Viscosity in strongly interacting
1195 quantum field theories from black hole physics. *Phys. Rev. Lett.*, 94:111601,
1196 Mar 2005.
- 1197 [24] Fred Cooper and Graham Frye. Single-particle distribution in the hydro-
1198 dynamic and statistical thermodynamic models of multiparticle production.
1199 *Phys. Rev. D*, 10:186–189, Jul 1974.
- 1200 [25] Adam Kisiel. Nonidentical-particle femtoscopy at $\sqrt{s_{\text{NN}}} = 200 \text{ GeV}$ in hy-
1201 drodynamics with statistical hadronization. *Phys. Rev. C*, 81:064906, Jun
1202 2010.
- 1203 [26] Adam Kisiel and David A. Brown. Efficient and robust calculation of femto-
1204 scopic correlation functions in spherical harmonics directly from the raw
1205 pairs measured in heavy-ion collisions. *Phys.Rev.*, C80:064911, 2009.
- 1206 [27] S. Pratt. Pion Interferometry for Exploding Sources. *Phys.Rev.Lett.*, 53:1219–
1207 1221, 1984.

- 1208 [28] S.V. Akkelin and Yu.M. Sinyukov. The HBT-interferometry of expanding
1209 inhomogeneous sources. *Z.Phys.*, C72:501–507, 1996.
- 1210 [29] A. Kisiel, M. Galazyn, and P. Bozek. Pion, kaon, and proton femtoscopy in
1211 Pb–Pb collisions at $\sqrt{s_{NN}}=2.76$ TeV modeled in 3+1D hydrodynamics. 2014.
- 1212 [30] K. Aamodt et al. Two-pion Bose-Einstein correlations in central Pb-Pb colli-
1213 sions at $\sqrt{s_{NN}} = 2.76$ TeV. *Phys.Lett.*, B696:328–337, 2011.
- 1214 [31] V.M. Shapoval, P. Braun-Munzinger, Iu.A. Karpenko, and Yu.M. Sinyukov.
1215 Femtoscopy correlations of kaons in $Pb + Pb$ collisions at LHC within hy-
1216 drokinetic model. 2014.
- 1217 [32] TORQUE Resource Manager - An open source resource manager
1218 providing control over batch jobs and distributed compute nodes
1219 <http://www.adaptivecomputing.com/products/open-source/torque/>.

₁₂₂₀ List of Figures

1221 1.1	The Standard Model of elementary particles [1].	3
1222 1.2	A string breaking and a creation of a new quark-anti-quark pair [4].	5
1223 1.3	The coupling parameter α_s dependence on four-momentum trans-	
1224 fer Q^2 [5].	6	
1225 1.4	The QCD potential for a quark-antiquark pair as a function of dis-	
1226 tance for different temperatures. A value of a potential decreases		
1227 with the temperature [4].	7	
1228 1.5	A number of degrees of freedom as a function of a temperature [7].	7
1229 1.6	Phase diagram coming from the Lattice QCD calculations [8]. . .	8
1230 1.7	Left: stages of a heavy ion collision simulated in the UrQMD	
1231 model. Right: schematic view of a heavy ion collision evolution [8].	9	
1232 1.8	Overlapping region which is created in heavy ion collisions has an	
1233 almond shape. Visible x-z plane is a <i>reaction plane</i> . The x-y plane is		
1234 a <i>transverse plane</i> . The z is a direction of the beam [11].	11	
1235 1.9	Cross-section of a heavy ion collision in a transverse plane. The	
1236 b parameter is an <i>impact parameter</i> - a distance between centers of		
1237 nuclei during a collision. An impact parameter is related with the		
1238 centrality of a collision and a volume of the quark-gluon plasma [12].	12	
1239 1.10	<i>Lower:</i> The elliptic flow v_2 follows the hydrodynamical predictions	
1240 for an ideal fluid perfectly. Note that > 99% of all final hadrons		
1241 have $p_T < 1.5 \text{ GeV}/c$. <i>Upper left:</i> The v_2 plotted versus transverse		
1242 kinetic energy $KE_T = m_T - m_0 = \sqrt{p_T^2 + m_0^2} - m_0$. The v_2 follows		
1243 different universal curves for mesons and baryons. <i>Upper right:</i>		
1244 When scaled by the number of valence quarks, the v_2 follows the		
1245 same universal curve for all hadrons and for all values of scaled		
1246 transverse kinetic energy [13].	13	
1247 1.11	Invariant yield of particles versus transverse mass	
1248 $m_T = \sqrt{p_T^2 + m_0^2}$ for π^\pm , K^\pm , p and \bar{p} at mid-rapidity for p+p		
1249 collisions (bottom) and Au+Au events from 70-80% (second		
1250 bottom) to 0-5% (top) centrality [14].	14	

1251	1.12 Thermal photons spectra for the central Au+Au collisions at	
1252	$\sqrt{s_{NN}} = 200$ GeV computed within different hydrodynamical	
1253	models compared with the pQCD calculations (solid line) and	
1254	experimental data from PHENIX (black dots) [15].	15
1255	1.13 Left: Invariant mass spectrum of e^+e^- pairs in Pb+Au collisions	
1256	at 158A GeV compared to the sum coming from the hadron decays	
1257	predictions. Right: The expectations coming from model calcula-	
1258	tions assuming a dropping of the ρ mass (blue) or a spread of the	
1259	ρ width in the medium (red) [16].	16
1260	1.14 Azimuthal angle difference $\Delta\phi$ distributions for different colliding	
1261	systems at $\sqrt{s_{NN}} = 200$ GeV. Transverse momentum cut: $p_T > 2$	
1262	GeV. For the Au+Au collisions the away-side jet is missing [17]. . .	17
1263	2.1 The cascade decay in the single freeze-out model. An unstable res-	
1264	onance x_N is formed at the freeze-out hypersurface and travels for	
1265	the time τ_N depending on its lifetime and decays. If the products	
1266	are also resonances (x_{N-1}, x_2) they decay further until the stable	
1267	particles are formed (x_1) [18].	24
1268	3.1 Bertsch-Pratt direction naming convention used in heavy ion col-	
1269	lision.	26
1270	3.2 The pair wave function is a superposition of all possible states. In	
1271	case of particle interferometry it includes two cases: particles with	
1272	momenta p_1, p_2 registered by detectors A, B and p_1, p_2 registered	
1273	by B, A respectively.	27
1274	3.3 An averaged three-dimensional Gaussian source function with dif-	
1275	ferent widths was averaged into one-dimensional function. To il-	
1276	lustrate deformations, one-dimensional Gaussian distribution was	
1277	fitted.	30
1278	3.4 Correlation function width dependence on total pair momentum.	
1279	Pion pairs with a large total momentum have a wider correlation	
1280	(smaller apparent source) [27].	34
1281	4.1 Spherical harmonics coefficients of the two-pion correlation func-	
1282	tion. From the top left: $\Re C_0^0$, $\Re C_2^0$ and $\Re C_2^2$. Only few centrality	
1283	bins are presented for increased readability.	37
1284	4.2 Spherical harmonics coefficients of the two-kaon correlation func-	
1285	tion. From the top left: $\Re C_0^0$, $\Re C_2^0$ and $\Re C_2^2$. Only few centrality	
1286	bins are presented for increased readability. The $\Re C_2^2$ is noisy, but	
1287	one can still notice that it differs from zero and is becoming negative. 38	

1288	4.3 Spherical harmonics coefficients of the two-proton correlation function. From the top left: $\Re C_0^0$, $\Re C_2^0$ and $\Re C_2^2$. Only few centrality bins are presented for increased readability. The $\Re C_2^0$ and $\Re C_2^2$ are noisy, but one can still notice, that they differ from zero and are becoming positive.	39
1289		
1290		
1291		
1292		
1293	4.4 One-dimensional correlation function for pions (top left), kaons (top right) and protons (bottom) for different centralities.	40
1294		
1295		
1296		
1297		
1298	4.5 One-dimensional correlation functions for pions, kaons and protons, for the same centrality bin and different k_T ranges. The plot was zoomed in to the region which illustrates the k_T dependence in the best way. Only few of the calculated ranges are presented for better readability.	41
1299		
1300		
1301	4.6 Femtoscopic radii in LCMS coming from two-pion correlation functions for all centrality bins as a function of m_T . The dashed lines are power-law fits. The most central collisions (0-5%) are compared to the results from ALICE [30]. The two datasets are shifted to the right for visibility [29].	42
1302		
1303		
1304		
1305	4.7 Femtoscopic radii extracted from two-kaon correlation functions for different centrality bins as a function of m_T . [29].	43
1306		
1307	4.8 Femtoscopic radii extracted from two-proton correlation functions for different centrality bins as a function of m_T . [29].	44
1308		
1309	4.9 The results from the calculations for the pions, kaons and protons in for the three centralities presented on the common plot. One can notice that radii for particular centralities and different particle types follow the common power-law scaling. [29].	45
1310		
1311		
1312		
1313	4.10 Top left: one-dimensional radius for pions, kaons and protons calculated in the PRF. Top right: the R_{inv} scaled by the proposed factor. Bottom: averaged one-dimensional radius in the LCMS for pions, kaons and protons. Only three centrality bins are shown for the better readability [29].	46
1314		
1315		
1316		
1317		